

# Cluster observations of an intense normal component of the electric field at a thin reconnecting current sheet in the tail and its role in the shock-like acceleration of the ion fluid into the separatrix region

J. R. Wygant,<sup>1</sup> C. A. Cattell,<sup>1</sup> R. Lysak,<sup>1</sup> Y. Song,<sup>1</sup> J. Dombeck,<sup>1</sup> J. McFadden,<sup>2</sup> F. S. Mozer,<sup>2</sup> C. W. Carlson,<sup>2</sup> G. Parks,<sup>2</sup> E. A. Lucek,<sup>3</sup> A. Balogh,<sup>3</sup> M. Andre,<sup>4</sup> H. Reme,<sup>5</sup> M. Hesse,<sup>6</sup> and C. Mouikis<sup>7</sup>

Received 28 July 2004; revised 15 February 2005; accepted 8 April 2005; published 3 September 2005.

[1] Measurements from the Cluster spacecraft of electric fields, magnetic fields, and ions are used to study the structure and dynamics of the reconnection region in the tail at distances of  $\sim 18 R_E$  near 22.4 MLT on 1 October 2001. This paper focuses on measurements of the large amplitude normal component of the electric field observed in the ion decoupling region near the reconnection x-line, the structure of the associated potential drops across the current sheet, and the role of the electrostatic potential structure in the ballistic acceleration of ions across the current sheet. The thinnest current sheet observed during this interval was bifurcated into a pair of current sheets and the measured width of the individual current sheet was 60–100 km ( $3\text{--}5 c/\omega_{pe}$ ). Coinciding with the pair of thin current sheets is a large-amplitude ( $\pm 60$  mV/m) bipolar electric field structure directed normal to the current sheets toward the midplane of the plasma sheet. The potential drop between the outer boundary of the thin current sheet and the neutral sheet due to this electric field is 4–6 kV. This electric field structure produces a 4–6 kV electric potential well centered on the separatrix region. Measured  $H^+$  velocity space distributions obtained inside the current layers provide evidence that the  $H^+$  fluids from the northern and southern tail lobes are accelerated into the potential well, producing a pair of counterstreaming, monoenergetic  $H^+$  beams. These beams are directed within 20 degrees of the normal direction with energies of 4–6 keV. The data also suggest there is ballistic acceleration of  $O^+$  in a similar larger-scale potential well of 10–30 kV spatially coinciding with the larger scale size ( $\sim 1000\text{--}3000$  km) portions of current sheet surrounding the thin current sheet. Distribution functions show counterstreaming  $O^+$  populations with energies of  $\sim 20$  keV accelerated along the average normal direction within this large-scale potential structure. The normal component of the electric field in the thin current sheet layer is large enough to drive an  $\mathbf{E} \times \mathbf{B}$  drift of the electrons  $\sim 10,000$  km/s ( $0.25 \times$  electron Alfvén velocity), which can account for the magnitude of the cross-tail current associated with the thin current sheet.

**Citation:** Wygant, J. R., et al. (2005), Cluster observations of an intense normal component of the electric field at a thin reconnecting current sheet in the tail and its role in the shock-like acceleration of the ion fluid into the separatrix region, *J. Geophys. Res.*, **110**, A09206, doi:10.1029/2004JA010708.

<sup>1</sup>School of Physics and Astronomy, University of Minnesota, Minneapolis, Minnesota, USA.

<sup>2</sup>Space Sciences Laboratory, University of California, Berkeley, California, USA.

<sup>3</sup>Blackett Laboratory, Imperial College, London, UK.

<sup>4</sup>Swedish Institute of Space Physics, Uppsala Division, Uppsala, Sweden.

<sup>5</sup>Centre d'Etude Spatiale des Rayonnements, Toulouse, France.

<sup>6</sup>NASA Goddard Space Flight Center, Greenbelt, Maryland, USA.

<sup>7</sup>University of New Hampshire, Durham, New Hampshire, USA.

## 1. Introduction

[2] In this paper, we investigate the structure of electric and magnetic fields responsible for the acceleration of ion beams, the formation of the electron current layer, and the flow of Poynting flux during the process of magnetic field line reconnection in the decoupling region in the Earth's geomagnetic tail. Magnetic field line reconnection in collisionless magnetized plasmas involves the release of magnetic field energy present in stressed magnetic field configurations and its conversion into outgoing energy flux. This energy flux can be in the form of ion jets [Hones, 1979; Paschmann et al., 1979; Sonnerup et al., 1981; Phan

*et al.*, 1996; *Phan and Paschmann*, 1996], outflowing populations of electrons [*Scudder et al.*, 2002], and radiated wave energy [*Song and Lysak*, 1995]. One of the principal experimentally documented forms of energy flux in the Earth's magnetosphere observed during reconnection is ion jets. Statistical studies indicate that bursty bulk flows (BBFs) of ions generally attributed to reconnection jets are a major agent for the transport of energy in the tail [*Angelopoulos et al.*, 1994] during active conditions. Despite the extensive theoretical and experimental interest in this process, there has never been a direct comparison between the measured electric and magnetic field structures near the reconnection x-line and the distribution functions of the accelerated ion populations. The nature of the specific structure of the reconnection region near the x-line/decoupling region where shock-like structures are believed to form and phase stand in the incoming flow is still an outstanding problem of space plasma physics. Most modern models of reconnection find their origins in the scenario provided by *Petschek* [1964]. Petschek divided the reconnection geometry into several regions. The first is a region of inflowing magnetic field lines and plasma which obey the frozen-in condition and  $\mathbf{E} \times \mathbf{B}$  toward the current layer. In Petschek's geometry, the current layer bifurcates into two layers that are back-to-back slow mode shocks which phase stand in the flow of plasma toward the current layer. These slow mode shocks are associated with jump conditions, which describe the decrease in the tangential component of the magnetic field, the conservation of the normal component of the magnetic field, the jump in density, and the acceleration of plasma away from the x-line due to magnetic tension (the MHD Walen condition). At the center of the reconnection region is a small-scale volume in which classical MHD is violated; therefore magnetic field lines are decoupled from the plasma and "diffuse" through the fluid to reconnect in a new topological configuration. The mechanisms responsible for ion and electron decoupling from the magnetic field and the spatial scales over which they occur are all matters of strong experimental and theoretical interest. In most theoretical scenarios, the ion decoupling occurs on a scale size typically comparable to an ion inertial length, and the electron decoupling occurs within a smaller region embedded within the ion-decoupling region. MHD provides no information on the precise nature of this decoupling, the structure of the fields, how particles are accelerated through the structure, or how decoupling occurs. MHD imposes a series of conservation laws on the large-scale reconnection structure but does not prescribe the precise mechanism by which the individual particles and constituent fluids satisfy them. In fact, the precise mechanism(s) may vary from one plasma regime to another. In this paper, we focus specifically on the structures responsible for ion decoupling and acceleration and leave the important issue of the smaller scale electron decoupling to later work. (The paper will, however, provide insight into the structures influencing the nature of the electron flows near the x-line, including very large  $\mathbf{E} \times \mathbf{B}$  drifts.) Mechanisms proposed for ion decoupling have included (1) current driven micro-instabilities which can scatter both electrons and ions or (2) stochastic, meandering, or Speiser orbits of nonadiabatic ions displaced along the reconnection electric field in the small scale reversed magnetic field [*Speiser*, 1965; *Cowley*,

1986; *Hughes*, 1995]. In this paper, we provide evidence for a coherent single-step ion acceleration into the region between the standing wave/current sheets due to a small-scale shock-like electric field, which exists normal to the current layers/standing waves within several ion inertial lengths of the x-line.

[3] Recently, *Mozer et al.* [2002], using data from the Polar spacecraft at the front side magnetopause during a reconnection event, presented the first observations of a strong bipolar normal component of the electric field which correlates with the Hall magnetic field perturbation. The scale size of this structure and the associated current sheet observed by Mozer and coworkers was  $\sim 6 c/\omega_{H+}$ . Recent observations from Cluster in the tail [*Wygant et al.*, 2003] show that similar current structures with the associated bipolar electric field structures can occur on very small scale sizes ( $3-5 c/\omega_{pe}$ ) over which incident ions are non-adiabatic. The data from other Cluster spacecraft, which encounter the same current sheet at a distance 2000 km earthward (in the outflow direction), show the current sheet and associated current sheet have broadened in a manner consistent with the diverging geometry of Petschek-like standing waves. At this downstream location, the width is on the order of  $20-40 c/\omega_{pe}$ . The opening angle for the standing waves is  $10-20$  degrees. The normal component of the electric field can be quite intense, producing significant potential drops across the current layers. The data presented here provide the first experimental evidence that a primary agent in the decoupling of the ions is the normal component of the electric field at thin current layers. The normal component of the electric field is much larger than the tangential component of the electric field. The value of the tangential component of the electric field has long been a subject of interest since it is strongly associated with normal mass flow and Poynting flux into the reconnection region. The normal component plays a different role. The normal component is an electrostatic "charge separation" electric field coupling the electron fluid to the ion fluid. It may be regarded as the longitudinal component of the small scale electromagnetic shock-like structures which phase stand in the incoming reconnection fluid flow. The data provide evidence that a potential well coinciding with the magnetic field reversal is responsible for acceleration of the incident ions through the current layer near the x-line. This energization process produces counterstreaming ion beams in the separatrix region. Since the ions traverse potential well in a small fraction of a gyroperiod, this scenario suggests the ions may bounce in the well and be quasi-trapped on scales much smaller than an ion inertial length. The existence of these counterstreaming beams motivates the suggestion that the particle pressure associated with the counterstreaming beams is responsible for the major contribution to pressure balance inside the diamagnetic cavity near the ion decoupling region. The data suggest a conceptual scenario in which the normal component of the electric field plays somewhat different roles depending on whether it is analyzed within the context of the individual ion motion or the fluid picture. In the individual particle picture, it accelerates particles into the regions between the separatrices and is the major force in confining them. Another smaller contribution to confining the ions may be magnetic gyration out side the potential well. In the ion fluid picture,

the normal electric field balances the sum of the ion pressure gradient and the fluid convective derivative. Thus individual ions are accelerated into the separatrix region, while in the fluid picture, ion fluid elements are decelerated as they transit the standing structure due to the dominance of the pressure gradient over the electric field. In summary, the data suggest that the structure of the potential well and the acceleration of the ion fluid through it play important roles in controlling the density profile, the normal reconnection flow velocity profile, pressure balance in the current layer diamagnetic cavity, energy outflow, and entropy. Since the normal flow velocity controls the reconnection rate, it can be argued that the dynamics of the acceleration, confinement, and ejection of ions plays a central role in governing the rate of reconnection. The data also suggest the  $\mathbf{E} \times \mathbf{B}$  drift of the electrons is a major contributor near the x-line to the current intensity responsible for small-scale magnetic shear. Under the limiting condition that the  $\mathbf{E} \times \mathbf{B}$  drift of the electrons provides all of the current, Ampere's law gives the relation that the potential drop across the current layer is  $\phi \sim \Delta B^2/4\pi ne$ , where  $n$  is the total number of electron charge carriers. For the specific example of the thin current sheet presented herein, the magnitude of potential drop determined from the electric field measurement is roughly equal to this theoretical limit. This value of the potential drop is such that any ion with mass  $m_i$ , which is accelerated through the potential drop, will increase its kinetic energy by  $(1/2)m_i V^2$ , where  $V$  is  $B/(4\pi nm_i)^{1/2}$ . This acceleration is along the normal direction. Thus in the region near the immediate vicinity of the x line, where the evidence suggests current sheets can be especially thin, the ion acceleration is dominated by electrostatic forces. These forces arise from the Lorentz force on the electron fluid, which accelerates the electron current layer towards the center of the reconnection region. The ions are coupled to the electrons by the charge separation electric field preserving quasi-neutrality. Since the electrons have small inertia compared with the ions, the electron force equation gives  $(1/ne) \mathbf{J}_e \times \mathbf{B} \sim \mathbf{E}_z$ . Integration of this relation across the current layer, provides another derivation, from the Force equation perspective, that  $\phi \sim \Delta B^2/4\pi ne$ . Note that the Lorentz force on the electron fluid,  $\mathbf{J}_{e \times B}$ , contains the familiar magnetic pressure term,  $\nabla(B^2/2\mu_0)$ , and magnetic tension term  $(\mathbf{B} \cdot \nabla)\mathbf{B}/\mu_0$ . Thus, these combined forces on the electrons are transmitted to the ions through the electrostatic field.

[4] This paper addresses only the electric field structure and particle acceleration scenario near (within several ion inertial lengths of) the x-line. It does not describe the situation at the current sheet farther from the x-line where ions may be more adiabatic in thicker current sheets in the MHD limit. In fact, much of the particle ion acceleration in the tail may occur over the more spatially extensive portion of the current sheet far from the x-line. Such ions may constitute the dominant contribution to the ion beams observed in the tail [Angelopoulos *et al.*, 1994]. The scenarios described within do not include complexities due to large- and small-scale instabilities which distort the current sheet geometry and produce time variable effects. Evidence from Cluster during this interval indicates that on larger scales, a low-frequency instability ( $10^{-2}$  Hz) operates to warp or kink the plasma sheet. On smaller scales, there is

evidence from the electric and magnetic field measurements for very intense waves ( $>100$  mV/m) in the general vicinity of the lower hybrid frequency (1–10 Hz) and also large-amplitude ( $\sim 50$  mV/m) solitary waves over timescales of  $\sim 1$  ms during the events presented herein [Cattell *et al.*, 2005]. Intense waves near the lower hybrid frequency appear regularly at the frontside magnetopause [Andre *et al.*, 2001; Bale *et al.*, 2002; Vaivads *et al.*, 2004] and in the tail [Cattell and Mozer, 1986; Cattell *et al.*, 1995] when and where reconnection occurs.

[5] There have been a number of studies of reconnection at the frontside magnetopause. There are a number of differences between the plasma conditions at the magnetopause and in the geomagnetic tail. There are two simplifying features of the geomagnetic tail in comparison to the front side magnetopause: (1) tail magnetic fields are more likely to be antiparallel and (2) the plasma in northern and southern lobes of the tail may have similar densities and temperatures, unlike the frontside magnetopause where there are often strong asymmetries. Magnetospheric plasma is typically much less dense and hotter than the magnetosheath plasma. Thus the structure of the reconnection region in the tail may often exhibit stronger symmetry than that at the frontside magnetopause. In addition, in the tail, plasma densities are typically about two orders of magnitude less than densities at the frontside magnetopause. This means that the important spatial scaling parameters, such as the Alfvén velocity, ion inertial length, and electron inertial lengths, are about an order of magnitude larger in the tail than at the frontside. This effectively increases the spatial resolution of the instrument measurements in the tail of structures scaling with these parameters. This is especially important for resolving the reconnection region with particle measurements, which reconstruct phase space using the spin (4 s) of the spacecraft. It should be noted that the parameter which appears to be related to the magnitude of the potential drop across the observed thin current layer,  $\phi \sim \Delta B^2/4\pi ne$ , is 1–2 orders of magnitude larger in the tail due to the extremely low densities ( $<0.1$  cm $^{-3}$ ) near the x-line. In our event, the incident upstream ions are comparatively cold ( $<100$  eV) due to their ionospheric origin. Thus acceleration of cold ions across a relatively large potential drop leads to striking mono-energetic beams in comparison to what would be expected at the frontside magnetopause.

[6] The dynamics of the reconnection region in the tail have several properties which can increase the probability of close encounters with the x-line of a spacecraft near the equatorial plane. The first is the observation that the reconnection region forms near the Earth during active periods and retreats down the tail as magnetic activity increases [Hones, 1979]. This implies that if the reconnection region forms earthward of a spacecraft at the Cluster position of  $18 R_E$ , it will often pass tailward over the position of the spacecraft. Another feature of the tail current sheet dynamics during active periods may enhance the probability of crossings near the x-line during candidate reconnection intervals. It is now clear that the tail current sheet can be strongly kinked over large scale during active periods and that these kinks propagate across the tail in a duskward direction with a period on the order of  $\sim 100$  s with wave lengths of tens of thousands of kilometers. As we shall discuss, these propagating kinks result in numerous



tail current sheet crossings over a nearly stationary spacecraft near the equatorial plane.

## 2. Previous Work

[7] Experimental studies using ion measurements from the Geotail spacecraft have provided clear evidence of the kinetic nature of the interaction of the ions with reconnection structures in the tail. A variety of different nonthermal distribution functions have been found, including distributions characteristic of particles meandering through current sheets in modified Speiser orbits, partial shell distributions accelerated in the downstream direction, and ion beams gyrating in the complex of magnetic and electric fields [Nagai *et al.*, 1998; Nakamura *et al.*, 1998; Hoshino *et al.*, 1998]. These distribution functions reflect the multiplicity of different acceleration mechanisms acting on different portions of ion phase space near the reconnection region. This paper is complementary to the previous observations since it presents for the first time experimental evidence for counterstreaming ion beams directed along current sheet normal near the x-line. Counterstreaming ion beams similar to those presented here have, however, been found in hybrid simulations. Of particular interest for the data we describe are a series of particle-in-cell simulations [Hoshino *et al.*, 1998, Plate 5] and hybrid simulations [Shay *et al.*, 1998, Figure 7; Arzner and Scholer, 2001, Figure 3, box 1] which provide evidence for counterstreaming  $H^+$  beams along the current sheet normal near the x-line. Both Shay and coworkers and Arzner and Scholer have discussed the cause of this acceleration in terms of the normal component of the electric field associated with the Whistler wave, which in their simulations mediate reconnection at small scales.

[8] A major result of recent observations in the tail is the documentation of thin current sheets with scale sizes on the order of an ion inertial length [Sergeev *et al.*, 1998; Runov *et al.*, 2003b]. Recent particle in cell, hybrid, and Hall MHD computer simulations of reconnection have emphasized the role of small-scale current structures ( $<c/\omega_{pi}$ ) near the x-line in decoupling ion and electron fluids and the role of smaller scale size structures ( $\sim c/\omega_{pe}$ ) for breaking the frozen-in condition for the electron fluid [Mandt *et al.*, 1994; Drake *et al.*, 1997; Drake *et al.*, 2003; Shay *et al.*, 1998; Hesse *et al.*, 1998; Kuznetsova *et al.*, 2001; Pritchett, 2001; Shay *et al.*, 2001; Hesse *et al.*, 2001]. Electromagnetic structures associated with whistler waves and kinetic Alfvén waves [Rogers *et al.*, 2001] have been proposed as candidates for mediating the reconnection process at small scales, where the large-scale MHD description of reconnection incorporating slow mode shocks is no longer appropriate. Within the context of dispersion relations of linear electromagnetic waves (i.e., current sheets mediating reconnection), it is expected that the ratio  $E$  should be on the order of an Alfvén velocity for current sheets large compared with an ion inertial length and much larger as the width becomes smaller (or  $k \perp$ , the wave normal component perpendicular to  $B$ , becomes larger). Analysis of dispersion relations for both kinetic Alfvén waves [Lysak, 1998] and Whistler waves [Gary, 1993] show that in the limit of small perpendicular spatial scales, the waves become strongly electrostatic with  $E_N/B_H \gg V_A$ , where the normal component of the electric field is equivalent to the component along the  $k$

vector and  $B_H$  is the transverse wave magnetic field perturbation. Thus within the context of linear waves, it is not surprising that at very thin current sheets the dynamics of the ions could be dominated by electrostatic forces.

[9] Laboratory experiments have been used to investigate the structure and dynamics of reconnection at thin current sheets with scale sizes on the order of electron inertial lengths [Stenzel *et al.*, 1982; Gekelman *et al.*, 1982; Stenzel *et al.*, 1983, and references therein]. The geometry of the magnetic field differed from that encountered here. Unlike the situation described herein, the laboratory magnetic field geometry was not anti-parallel but had a very strong imposed guide field ( $B_y$ ). However, some of the conclusions of those experiments are similar to the observations presented herein and flow from the dynamics of thin reconnection current sheets. Some of these features included (1) magnetized electrons and unmagnetized ion, (2) a general scenario in which the electrons are accelerated by the  $\mathbf{J} \times \mathbf{B}$  force and the ions are accelerated via coupling to the electrons by the (charge separation) electrostatic field and, (3) direct ballistic acceleration of the ions across the potential drop coinciding with the current layer. Since there is a very strong guide magnetic field in the laboratory experiment, much of the current supporting the magnetic shear is magnetic field-aligned. This is unlike the situation in the near anti-parallel geometry observed in the tail observations presented here, in which the  $\mathbf{E} \times \mathbf{B}$  drift of electrons supplies the current. The laboratory experiments have a geometry resembling that observed at the frontside magnetopause which has arbitrary angles between the magnetosheath and magnetospheric magnetic fields.

## 3. Measurements of the Cluster Spacecraft

### 3.1. Cluster Instrumentation

[10] The double probe Electric Field Wave (EFW) experiment [Gustafson *et al.*, 1997] provides two dimensional vector electric field measurements in the ecliptic plane ( $x$ - $y$  GSE plane) with an accuracy of 0.1 mV/m in the plasma sheet at a rate of 20 samples/s. The Magnetic Field Instrument (MFI) [Balogh *et al.*, 2001] provides three dimensional magnetic field vectors at a rate of 20 samples/s. The Cluster CIS CODIF [Reme *et al.*, 1997] provides three-dimensional  $H^+$  and  $O^+$  velocity space distribution functions every 8 s with a 4-s accumulation interval.

### 3.2. Coordinate Systems

[11] Two coordinate systems are discussed in this paper: the GSE system and the boundary normal system. The  $x$  GSE axis points from the Earth to the Sun. The  $y$  GSE axis lies in the ecliptic plane and points from dawn to dusk. The  $z$  GSE is orthogonal to the ecliptic, directed northward. In local reconnection coordinates used in this paper, the  $z$  axis is normal to the local current sheet surface, the  $x$  axis points in the direction of the reconnection outflow, and the  $y$  axis points along the local plasma sheet current flow direction (for an antiparallel geometry). The normal vector and the current sheet normal velocity have been determined from the relative timing between the four Cluster spacecraft. We have also used minimum variance analysis of the magnetic field variance tensor to determine the normal direction. These two independent methods provide estimates of the

normal vectors which are oriented within 20 degrees of one another. The normal vector estimates have an uncertainty which is primarily in the x-y gse plane, orthogonal to the ambient upstream magnetic field direction.

### 3.3. Overview of Current Sheet Crossings on 1 October 2001

[12] In this section, we provide a large scale context for the smaller scale observations to be presented. The reconnection region was encountered near  $\mathbf{R-gse} = (-16. R_E, 6.1 R_E, 5.0 R_E)$  in the premidnight sector during a major geomagnetic storm ( $Dst \sim -140$ , courtesy Kyoto World Data Center) on 1 October 2001. Approximately 40 plasma sheet/current layer crossings ( $\sim 10$  per spacecraft) were observed over the period from 0940 to 0955 UT while the spacecraft were close to the equatorial plane. The time interval of a major geomagnetic storm was specifically chosen on the supposition that this would produce the strongest and clearest signals for magnetic reconnection within Cluster apogee. An analysis of the ion flow data during this period (A. Roux et al., Dynamics of thin current sheets: Cluster observations, unpublished manuscript, 2004) showed an interval of tailward directed ion jetting followed by an interval of earthward jetting. As discussed earlier, this sequence of flows is a classic signature of a reconnection region passing tailward over the spacecraft [Hones, 1979]. Runov et al. [2003a] have presented observations of the large-scale structure ( $\sim 1000$  km) of the current sheet over the time interval 0947–0951 UT immediately after the crossing at 0946:46–0946:51 investigated herein. Runov and coworkers reported a number of important signatures of reconnection, including evidence for a bifurcated current sheet structure and quadrupole Hall magnetic field perturbations. Of special interest was the use of the four Cluster spacecraft to demonstrate the intimate relation between large-scale magnetic field line curvature (and magnetic tension) of newly reconnected field lines and the direction of ion jets ejected from the reconnection region.

[13] The large number of plasma sheet crossings observed during the 15-min interval from 0940 to 0955 UT was the consequence of a series of very large scale,  $\sim 100$  s, MHD fluctuations which carried the cross-tail current sheet over the spacecraft. The fluctuations resulted in about 40 complete and partial crossings observed cumulatively by the four Cluster spacecraft. Such fluctuations have previously been observed in the tail during substorm periods [Bauer et al., 1995]; however, their scale sizes could not be determined. The Cluster spacecraft are separated by about 2000 km in a tetrahedral array. Timing from the four Cluster spacecraft are used to determine the direction of the boundary normal, the velocity of the boundary normal, and spatial scales for these current sheet crossings. These MHD waves resulted in a “rocking” of the plasma sheet normal direction of about  $\pm 45$  degrees in the yz GSE plane consistent with propagation of the waves perpendicular to the ambient magnetic field producing large scale ripples in the current sheet. Since the data were obtained on 1 October 2001, the seasonal tilt of the magnetic equator relative to the y-z GSE plane was substantial. The seasonal tilt and the superposed MHD waves resulted in a sequence of current sheet encounters in which the normal vector

direction first pointed nearly in the z GSE direction followed by an encounter in which the normal vector contained a significant (0.7 to 0.9) y GSE component. An illustration of the large-scale waves is presented in Figure 2a. A more detailed discussion of the large scale structure of the current sheet is presented in section 3.6.2. Those current sheet crossings, which have a normal vector in the y GSE direction, allow the assessment of the normal component of the electric field since the measurement plane of the two dimensional electric field measurement is approximately in the x-y GSE plane. Recently, experimental evidence for the existence of current sheet waves similar to those presented here and a determination of their scale size and velocity of propagation has been presented by Zhang et al. [2002], Sergeev et al. [2003], and, Volwerk et al. [2003]. It has been suggested that these waves may be large-scale MHD kink modes. Theoretical analysis and simulations of kink modes may be found in the work of Karimabadi et al. [2003a, 2003b] and Pritchett and Coroniti [1996, 1997].

[14] An important property influencing reconnection structure and dynamics in the geomagnetic tail during magnetically active conditions is the ion composition. It has long been understood that ionospheric outflow of low energy ions is a major source of low energy ions in the plasma sheet during geomagnetic storms. During this interval, the CODIF instrument shows that there are often comparable contributions to the number density from both  $H^+$  and  $O^+$ . During the current sheet crossing studied in this paper, the CODIF instrument indicates the  $O^+$  density is  $\sim 0.07 \text{ cm}^{-3}$  and the  $H^+$  density is  $0.03 \text{ cm}^{-3}$ . Under these circumstances, the total upstream Alfvén velocity is 200–300 km/s, while the Alfvén velocity based on the  $H^+$  mass density (if the  $O^+$  is decoupled from the magnetic field line) is about  $\sim 1000$  km/s. The  $O^+$  inertial length is about 4000 km, while the  $H^+$  inertial length is  $\sim 1000$  km. The electron inertial length is about 20 km. The plasma beta ranges from  $\ll 1$  in the asymptotic upstream tail lobe to 100–400 at the center of the diamagnetic cavity between the reconnection standing waves. The ion composition measurements indicate that most of the pressure is provided by the  $O^+$  ions. The beta at the center of the current sheet is determined from the ratio of the magnetic field pressure inside and outside the diamagnetic cavity.

### 3.4. Observations at a Very Thin Current Sheet

[15] This section presents measurements from Cluster Spacecraft 4 through a very thin (100 km half width) current sheet. The fact that the Poynting flux and the x component of the flow velocity observed by the Cluster spacecraft were directed earthward is strong evidence that the x-line located tailward of the Cluster spacecraft. Since Spacecraft 4 was the most tailward, it was closest to the x-line. This spacecraft observed the smallest-scale current sheet, the strongest normal component of the electric field, an electrostatic potential well straddling the small-scale current layer, and evidence that  $H^+$  ion beams have been nearly ballistically accelerated into this electrostatic potential well. Evidence that  $O^+$  ions are accelerated by a larger-scale potential well coinciding with the surrounding large-scale current sheet is presented. Spacecraft 3 was about 2000 km further down-

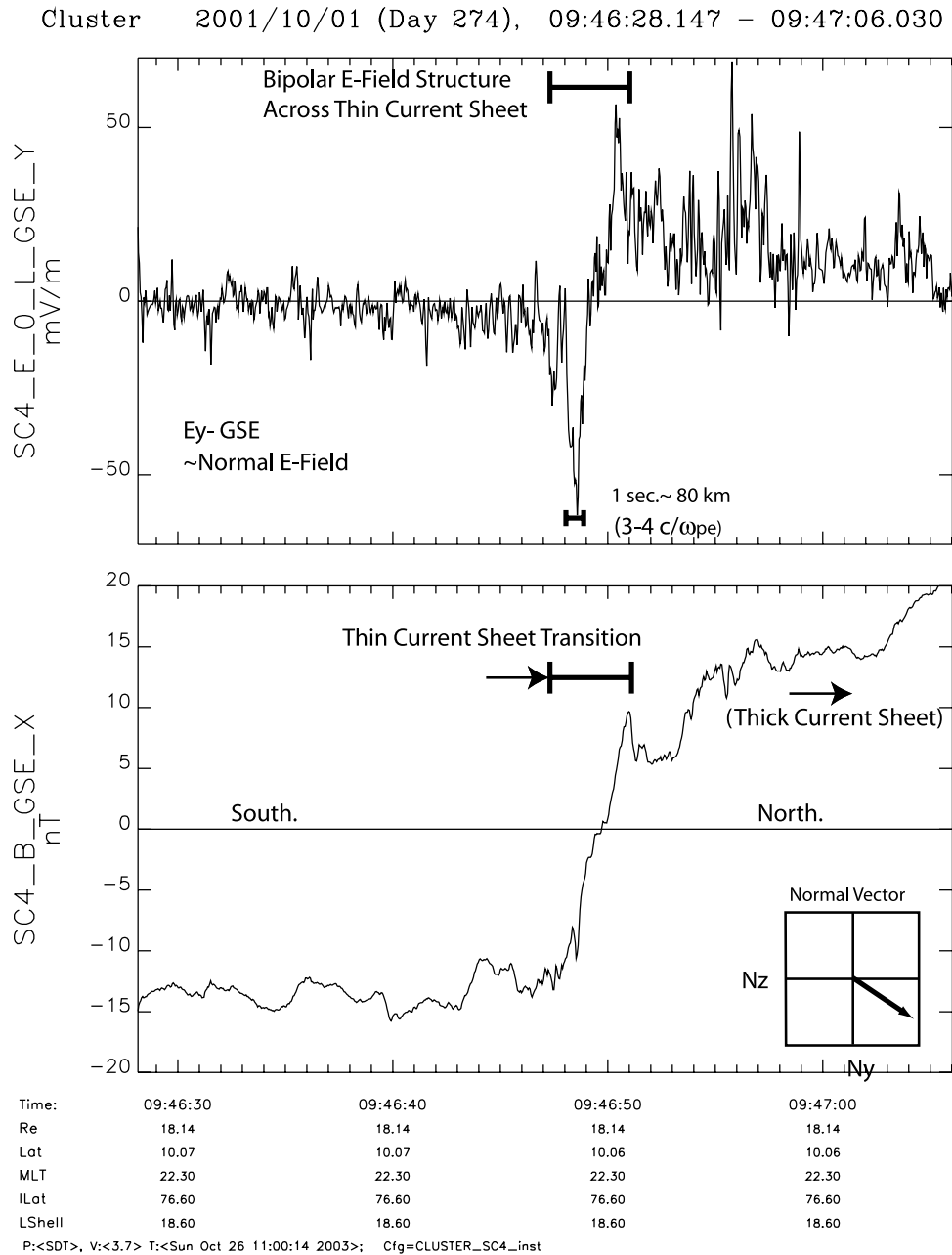


**Figure 1.** Electric and magnetic field data from the Cluster spacecraft 4 from a “thin” ( $\Delta L \sim 4c/\omega_{pe}$ ) current sheet on 1 October 2001 at 0946:50 UT. Measurements are (top) Ey-GSE dominated by the normal component of the electric field and (bottom) Bx GSE showing current sheet. The normal vector is  $(-0.05, 0.80, -0.59)$ . The normal vector is within 37 degrees of the y GSE direction. Distance scale determined from normal velocity,  $V_n \sim 80$  km/s.

stream (in x GSE direction and closer to the Earth) from Spacecraft 1. This spacecraft observed smaller electric fields over a larger region (500 km) coinciding with a broader current sheet closer to MHD scales. Spacecraft 1 was displaced in the z GSE direction. It encountered only a portion of the southern portion of the large-scale current sheet on a somewhat “skimming” trajectory. Spacecraft 2 encountered the crossing also at a downstream position relative to Spacecraft 4. The Spacecraft 2 electric field data were obtained through an analog channel that was not

filtered so that the waveform may be aliased. There is no ion data from Spacecraft 2.

### 3.5. Evidence for a Strong Potential Drop Across Very Thin Current Sheets (3–5 $c/\omega_{pe}$ ) and Formation of a Potential Well for Ions

[16] Electric field and magnetic field measurements from the thinnest current sheet obtained during the 0940–0950 UT time are presented in Figure 1. The top part is the y GSE component of the electric field and the bottom part is

Schematic of current sheet  
surface wave (yz gse projection)  
10/01/01 9:45 to 9:50 UT

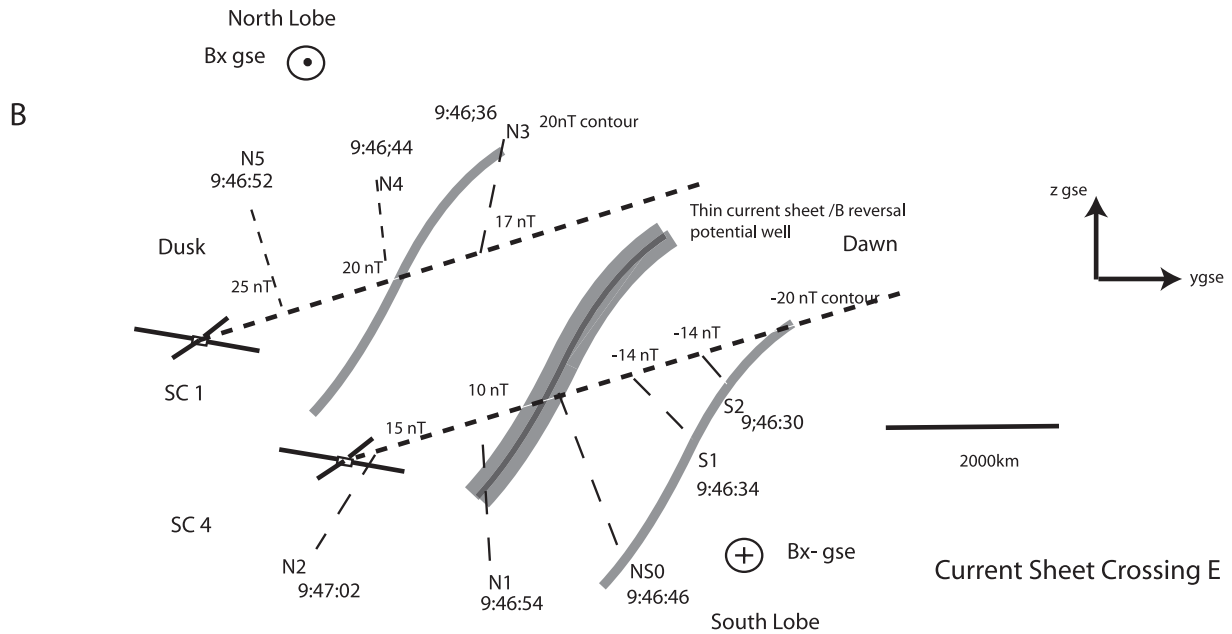
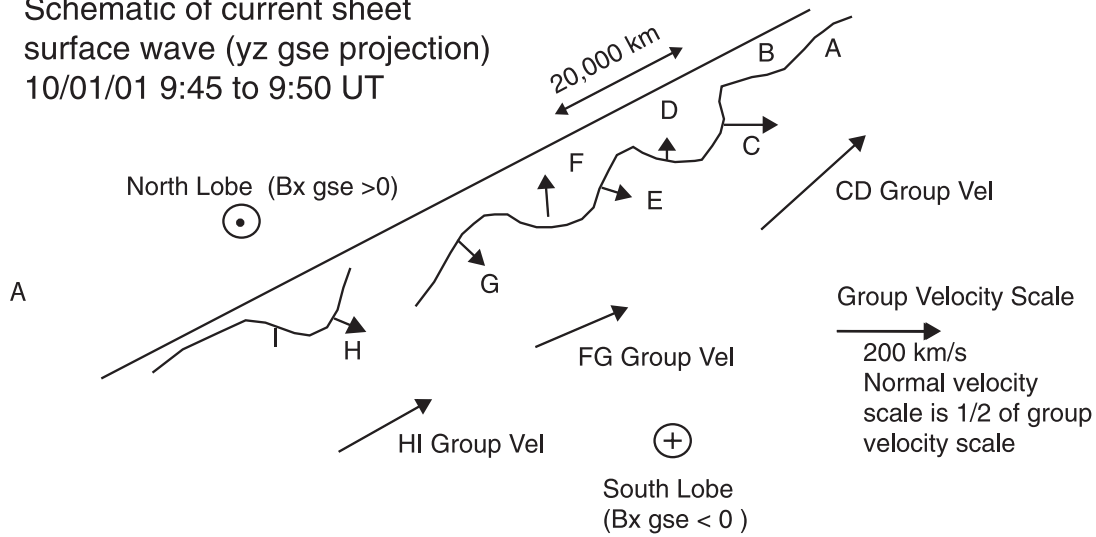


**Figure 2.** (a) Schematic of large-scale ( $\sim 100$  s) current sheet fluctuations. Boundary normal vectors labeled by letter. Data in figure corresponds to crossing E. (b) Schematic of Spacecraft 1 and 4 skimming relative to warped current sheet in z-y gse plane during crossing E. Times and numbers refer to times of distribution functions. Velocity of SC along world line relative to current sheet  $\sim 200$  km/s. Normal velocity  $\sim 80$  km. Values of local magnetic field magnitude (nT) and times of distribution functions are given along trajectory.

the x GSE component of the magnetic field. The magnetic field vector is dominated by the x GSE component, which shifts from negative to positive in a period of about 2 s as the cross-tail current sheet passes over the spacecraft. Initially, the spacecraft is located in the southern tail lobe region with the magnetic field directed away from the Earth. Notice that there is a sharp transition in the  $B_x$  GSE =  $-15$  nT at 0946:47 to  $B_x$  GSE =  $10$  nT at 0946:51 UT. This jump is consistent with a passage through a large fraction of the cross-tail

current system over 2 s. This current sheet is imbedded in a broader current sheet indicated by a gradual increase in  $B_{x\text{gse}}$  from 15 nT to 30 nT over a period of 20 s following the thin current sheet encounter. The initial portion of this rise may be seen in Figure 1. The electric field has a bipolar signature coinciding with the flip in the direction of the magnetic field. The electric field reversal occurs at the center of the current sheet. The electric field magnitude peaks at about  $\pm 60$  mV/m. The measured electric field component is primarily in the

Tail X-Line Crossing October 1, 2001

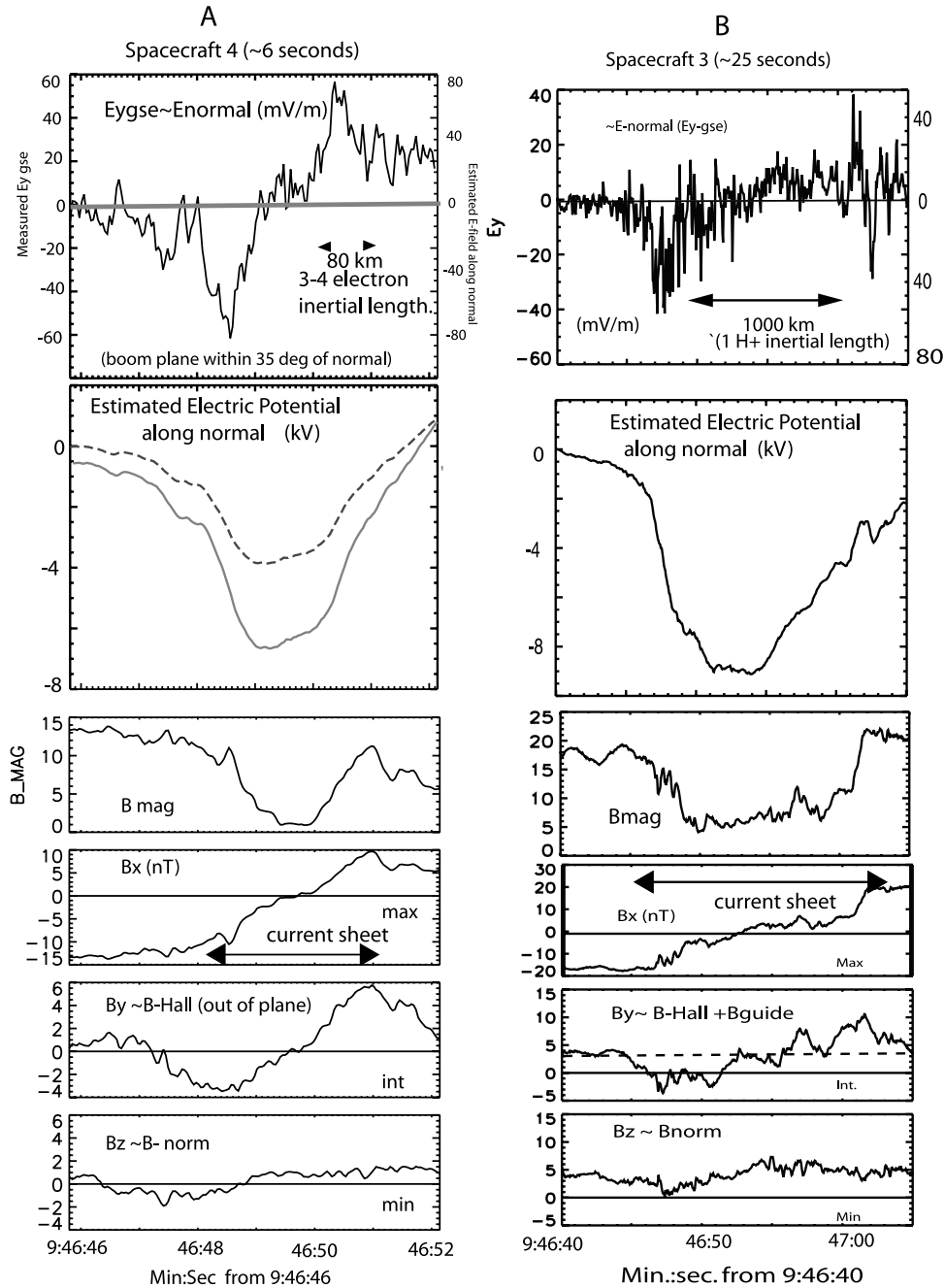


**Figure 3.** (a) SC 4 and (b) SC 3 electric field ( $E_y$  GSE), estimated electric potential drop (showing potential well), magnetic field magnitude, three components of magnetic field vector in boundary normal coordinate system determined from magnetic variance analysis:  $B_x$  (in normal or minimum variance direction),  $B_y$  (intermediate- Hall perturbation), and  $B_z$  (maximum variance direction- maximum current sheet shear).

direction normal to the current sheet. A schematic of the current sheet and the spacecraft trajectory relative to the current sheet is presented in Figure 2. The normal vector in GSE coordinates as determined by timing between the four spacecraft is  $(-0.05, 0.80, -0.59)$ . The projection of this vector in the  $ny$ - $nz$  GSE plane is presented in the top part of Figure 2. As discussed in the next section, minimum variance analysis was also used to determine the direction of the normal to the small-scale current sheet.

The normal determined using magnetic minimum variance analysis is  $(0.03, 0.84, -0.55)$ . The ratio of the intermediate to minimum eigenvalue of the magnetic variance tensor was  $>10$  and a visual inspection of Figure 3 indicates a quasi-coherent magnetic structure with a robust Hall magnetic field signature, providing confidence in the minimum variance analysis. The uncertainties in the normal direction determined by these two different methods are sufficiently small that we can be confident in the direction



**Table 1.** Relative Position of Cluster Spacecraft in Kilometers (GSE) (Spacecraft # 1 at Origin)

	X	Y	Z
Spacecraft 2	−50.	1990.	130.
Spacecraft 3	590.	1120.	−1650.
Spacecraft 4	−1550.	1260.	−990.

of the normal to  $\sim 20$  degrees. Thus during this crossing, a large component of the normal to the current sheet was directed in the +y GSE direction. The velocity of the current sheet along the normal direction is 60–100 km/s. Since the passage from the center of the current sheet at 0946:50 to the outer edge of the current sheet at 0946:51 required approximately 1 s, the half width of the current sheet is  $\Delta L_C \sim 100$  km. Using the electron density estimate of  $n \sim 0.1 \text{ cm}^{-3}$  from the spacecraft potential (consistent with density from the ion composition experiment), the width is  $\Delta L_C \sim 3\text{--}5$  electron inertial lengths ( $c/\omega_{pe} \sim 20$  km). It is significantly thinner than the previously reported small-scale current sheets ( $\sim 40 c/\omega_{pe} \sim 1 c/\omega_{pH+}$ ) [Klecker *et al.*, 2003]. This is the thinnest current sheet (normalized to electron inertial lengths) of the crossings obtained during the interval from 0940 to 0950 UT interval and also the thinnest tail current sheet in the published literature. Recent observations by Andre *et al.* [2004] show that small-scale electric field structures exist at the frontside magnetopause along the current sheet.

[17] Given the measured direction of the normal vector, the measured y GSE component of the electric field is strongly dominated by the normal component of the electric field as observed in the rest frame of the current sheet. Under these circumstances, if the electric field measurement plane included the normal vector, the peak-to-peak amplitude of normal component of the electric field would be about  $\pm 85$  mV/m.

[18] Figure 3 presents an expanded view of the plasma sheet crossing of Figure 1 which compares  $E_{y\text{gse}}$  ( $\sim E$  normal), the estimated electric potential drop across the current sheet, the magnitude of the magnetic field, and three components of the magnetic field in boundary normal coordinates. The unit vectors of the boundary normal coordinate system have been determined from magnetic minimum variance analysis. The eigenvalues and eigenvectors of the magnetic field variance tensor are presented in Table 1.  $B_U$  (primarily in the x GSE direction) is the main field of the tail, showing the magnetic field reversal associated with the cross-tail current sheets.  $B_t$  is the magnetic field component along the intermediate eigenvector.  $B_t$  contains the Hall perturbation which is directed in the “out of plane” direction.  $B_N$  is the component of the magnetic field normal to the current sheet. (Tables 2–4).

[19] Figure 3 presents the estimated potential drop along the normal calculated from the spatial integration of the

**Table 2.** Boundary Normal Coordinates Spacecraft 1 Magnetic Minimum Variance Analysis 2001/10/01 0946:45.8 to 0946:52.13

	Eigenvector x GSE	Eigenvector y GSE	Eigenvector z GSE	Eigenvalue
$N_Z$	.03	.84	−.55	0.27 (min)
$N_Y$	.23	−.54	−.81	3.38 (int)
$N_X$	.97	.10	.21	70.2 (max)

**Table 3.** Normal to Current Sheet (GSE) Cluster Timing 2001/10/01 0946:40 to 0947:05

Nx	Ny	Ny	Normal Velocity
−0.05	0.80	−0.59	62–100 km/s

electric field along the normal across the small-scale current layer. The calculation shows the minimum of the potential well is centered on the magnetic field reversal. The potential well is 4–6 kilovolts deep relative to the outer boundary of the thin current sheet at roughly  $\pm 12$  nT. The width of one of the electrostatic walls of the potential well is on the order of 3–5 electron inertial lengths (100 km). The potential drop is calculated by converting temporal intervals to spatial distance along the current sheet normal by using the normal velocity of the current sheet as determined by timing from the four Cluster spacecraft. Lower and upper limits on this velocity were 60 and 100 km/s. Since the normal vector for the current sheet was approximately (but not completely) aligned with the measurement plane, the estimate “true” electric field in the normal direction is larger than the measured field by a factor of  $\sim 1.2$ . Error correction due to the Lorentz transformation between the measurement frame of the spacecraft and the Normal Incidence Frame (NIF) are about  $E_{\text{trans}} \sim V_{\text{pc}} \times B_{\text{max}} \sim 200 \text{ km/s} \times 15 \text{ nT} \sim 3 \text{ mV/m}$ . This is small compared with the observed 60 mV/m peak values and we assume, for the purposes of this calculation, the spacecraft frame coincides with the Normal Incidence Frame. We have also assumed that the tangential component of the electric field is negligible compared with the normal component of the electric field. The tangential component of the electric field is typically estimated to be  $\sim 0.1 V_A \times B$ , where  $V_A$  is the upstream Alfvén velocity based on the total mass density of  $H^+$  and  $O^+$  and  $B$  is the upstream magnetic field strength [Petschek, 1964; Birm *et*

**Table 4.** Plasma Parameters 10/01/01 0946:46–0946:51 Current Sheet Crossing (SC-40)

Parameter	Value	Comments <sup>a</sup>
B	1–12 nT	Center–Edge
$N_e$	$0.1 \text{ cm}^{-3}$	SC potential (1/2s ave)
$N_{H+}$	$0.03 \text{ cm}^{-3}$	6 s ave. thin current sheet
$N_{O+}$	$0.07 \text{ cm}^{-3}$	6 s ave. thin current sheet
$T_i$	100 eV	Thermal spread of beam
$T_e$	100–1 keV	Typical from dist functions
$L_C$	62–100 km ( $3\text{--}5 c/\omega_{pe}$ )	thin sheet thickness (center to edge)
$H^+$ Beam energy	5–6 keV	at center
$\beta$ at neutral sheet	1000	ratio of B-field tail lobe/diamagnetic cavity
$V_e$	$2 \times 10^4 \text{ km/s}$	typical 1 keV $e^-$
$V_{AH+}$	1000 km/s	$B^2/4\pi\rho_{H+}$ Edge (10 nT)
$V_{AO+}$	200 km/s	$B^2/4\pi\rho_{O+}$ Edge (10 nT)
$V_n$	60–100 km/s	Normal Vel current layer
$(c/\omega_{pe})$	20 km	Electron inertial length
$\Omega_{H+}$	0.15–0.015 Hz	edge–center
$r_{li}$ of beam	2000 km	(based on $V_i \sim 1000 \text{ km/s}$ at 5 nT)

<sup>a</sup>“Edge” refers to parameter measured at the outer edge of the thin current sheet where  $B \sim 10$  nT; “center” refers to center of neutral sheet where  $B \sim 1$  nT, “Ave. current sheet” refers to a 6 s average centered on the thin current sheet structure. This average includes intervals upstream of the thin current sheet.

al., 2001, and references within]. The validity of this estimate is supported by experimental measurements [Mozer et al., 1979; Mozer et al., 2002] as well as simulations under a wide variety of physical assumptions. If, however, locally the  $O^+$  ions are demagnetized inside the current layer, it is possible that the Alfvén velocity based exclusively on  $H^+$  mass density should be used. This value is locally on the order of 1000 km/s. For this event, then, the range of “local” Alfvén velocities that could be considered as appropriate for calculating the reconnection rate is  $V_A \sim 250$ –1000 km/s. The measured magnetic field range is  $B_{xgs} \sim 10$ –30 nT and the estimated  $E_{tan} \sim 0.25$ –4 mV/m. It should be noted that it is not clear that the asymptotic upstream region in the tail lobes where densities could be very low has been encountered by the Cluster spacecraft during this event and therefore estimates of the asymptotic Alfvén velocity and reconnection rates based on these values are not available. As we shall discuss later, estimates of  $E_{tan}$  based on  $H^+$  velocities measured upstream of the small-scale current sheets are on the order of several mV/m. It is sufficient for the purposes of this study that the estimates of tangential component of the electric field are significantly smaller than the measured large normal components of the electric field.

[20] An important reconnection signature, discussed in both the experimental and theoretical literature, is the Hall magnetic field perturbation,  $B_H$  [Sonnerup, 1979; Mandt et al., 1994; Nagai et al., 2001; Oieroset et al., 2001]. The data in the fifth show a bipolar Hall magnetic field perturbation with an amplitude of  $\sim 5$  nT or  $\sim 50\%$  of the in plane  $B_x$  component of the magnetic field. It is interesting to note the strong similarity between the bipolar waveform of the normal component of the electric field shown in the first part and the bipolar waveform of  $B_H$  displayed in the second part. This correlation is similar to that shown on larger spatial scales by Mozer and coworkers at the dayside magnetopause. The relative phase between these two electric and magnetic field components produces a contribution to the  $\mathbf{E} \times \mathbf{B}$  velocity which is directed in the positive x GSE direction and indicates that Spacecraft 4 is earthward of the reconnection x-line. This will be discussed more completely later during a detailed presentation of Figure 12 which shows estimates of the Poynting flux in the x and y directions and the  $\mathbf{E} \times \mathbf{B}$  velocity in the x and y directions. The x component of  $\mathbf{E} \times \mathbf{B}$  is an important diagnostic in this regard because the ion data (to be presented) indicate that Spacecraft 4 has intercepted the reconnection region sufficiently close to the x-line that the ion outflow velocity has not yet accelerated up to a full Alfvén velocity. Thus, it is important to have additional indicators that this is a reconnection event. The labels of the right-hand side of the bottom two  $\mathbf{E} \times \mathbf{B}$  velocity panels indicate the electron Alfvén velocity,  $B/(4\pi n m_e)^{1/2}$ . The component of the Poynting flux in the x direction is estimated from the two dominant terms in the calculation. It is given by  $S_x = E_y B_z - E_z B_y \sim -E_z B_y \sim -E_N B_H$  for the case in which  $E_N \sim 85$  mV/m  $\gg E_{TAN} < 5$  mV/m and  $B_H \sim 5$  nT  $\gg B_N \sim 1$  nT. The error is about .005 ergs/cm<sup>2</sup>s. The data show two layers of Poynting flux both directed in the positive y direction with a significant earthward component. The peak Poynting flux in the y direction is 0.4 to 0.7 ergs/cm<sup>2</sup>s. The peak earthward Poynting flux is

$\sim 0.4$  ergs/cm<sup>2</sup>s. The peak  $\mathbf{E} \times \mathbf{B}$  velocity in the y direction is about 6000 km/s. The peak earthward  $\mathbf{E} \times \mathbf{B}$  velocity estimated in this approximation is about 6000 km/s. These correspond to about 0.20  $V_{Ac}$ . The estimate of the  $\mathbf{E} \times \mathbf{B}$  velocity breaks down when  $B_x \sim 0$  nT near the magnetic field reversal due to error propagation effects, and in the case of the x component relative importance of  $E_{tan}$  compared with  $E_N$ . As we shall discuss, the electrons are magnetized and can participate in these large  $\mathbf{E} \times \mathbf{B}$  velocities. However, the bulk of the ions are unmagnetized and distribution functions indicate they are decoupled and have much smaller velocities ( $\sim 1000$  km/s). Thus the  $\mathbf{E} \times \mathbf{B}$  drift of electrons is an important contribution to the current layer. There is a strong gradient in the  $\mathbf{E} \times \mathbf{B}$  velocity at the inner edge of the current layer with the velocity decreasing from its peak value to zero over a distance along the normal of 0.1 s corresponding to  $\sim 10$  km or one half electron inertial length. The gyroradius of a 100 eV (or 6000 km/s) electron is about 10 km (in the  $B_x \sim 3$  nT field at the edge of the velocity shear) so that electrons may execute nonadiabatic orbits starting at this inner edge and continuing into the  $B_{xgsc} \sim 0$  region. Another issue of significance may be the role of this shear in driving the electron Kelvin-Helmholtz instability. This instability has been invoked as a dissipation mechanism in the electron diffusion region [Drake et al., 1997].

[21] The sixth part of Figure 3a shows the normal component of the magnetic field. The data show the normal component of the magnetic field is the most constant of the three magnetic components. It is on the order of  $\pm 1$  nT. Theoretically, for a steady-state, two-dimensional structure it should be constant and nonzero. However, inaccuracies in the minimum variance analysis due to violations of the two-dimensionality and steady state assumptions often produce a nonsteady normal magnetic field component.

[22] Figure 3b presents the electric and magnetic field measurements from Spacecraft 3 centered on the bifurcated current sheet structure on the magnetic field reversal due to the current layer in a similar format to that of Figure 1. The  $B_{xgsc}$  measurement shows that an appreciable portion of the transition between the southern and northern hemisphere tail lobe magnetic field direction is localized in two separated discrete current layers.  $B_{xgsc}$  jumps from  $-20$  nT to  $-4$  nT over 2 s between 0946:46 to 0946:48 UT. It increases more gradually from  $-4$  nT to about 7 nT over the next 12 s; and then jumps from 7 nT to 20 nT between 0947:01 UT and 0947:02 UT. The electric field in the y GSE direction is once again sampling a large fraction (80%) of the normal component of the electric field. The signature is bipolar with enhancements to  $-30$  mV/m at the first magnetic field jump and an enhancement to 20 mV/m in the second discrete jump. The sign of the electric field changes at about  $B_{xgsc} = 0$ . For the normal velocity of 80 km/s, the two discrete current sheets are separated by about 1000 km. We note that a significant portion of the electric potential drop is not confined to the thin current sheets but is distributed over the 700 km region between the two strong current layers. The depth of the potential well is  $\sim 9$  kV.

[23] Spacecraft 3 measurement of  $B_y$  shows a Hall magnetic field signature  $\pm 7$  nT superposed on a constant  $B_y$  ( $\sim 5$  nT). The dotted line corresponds to this constant  $B_y$  value that corresponds to a significant guide field. The guide magnetic field is much smaller in the observations

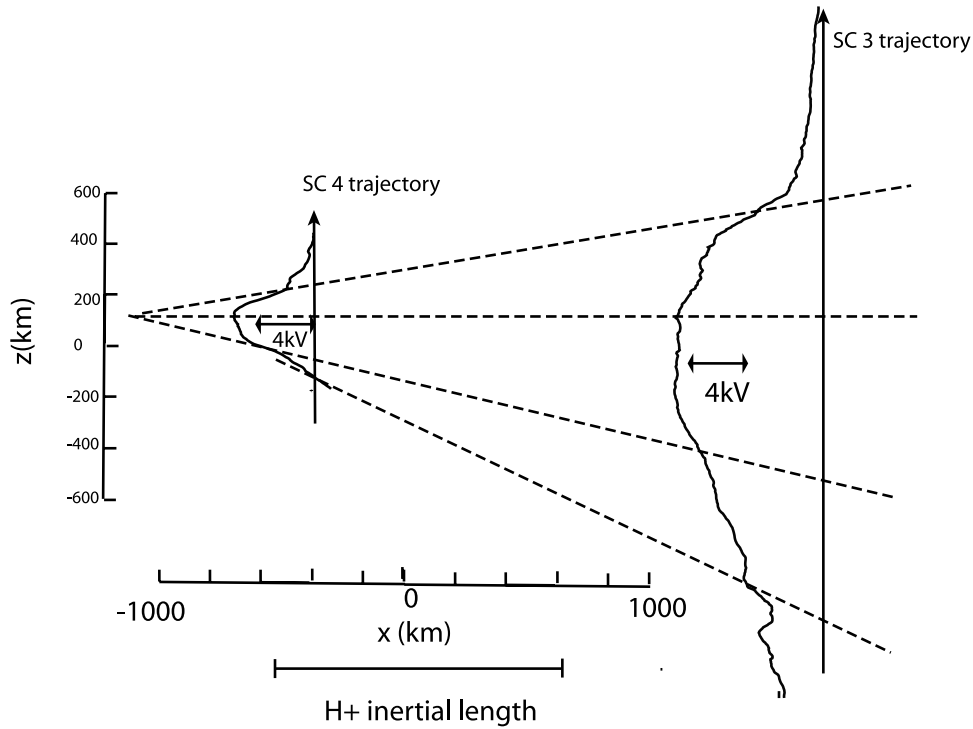


**Figure 4.** Diverging Petchek-like spatial structure of potential wells centered on magnetic field reversal near reconnection region from Cluster Spacecraft 3 and 4 electric field measurements.

from Spacecraft 4 closer to the x-line. Thus magnetic flux tubes are stressed such that an appreciable guide field present several ion inertial lengths from the x-line is not present much closer to the x-line.

[24] The waveform of the normal component of the electric field and the Hall magnetic field roughly correlate with a proportionality constant corresponding  $\sim 1000\text{--}4000\text{ km/s}$  which is significantly smaller than the value observed by Spacecraft 4 of  $10,000\text{--}15,000\text{ km/s}$ . This may be interpreted as the consequence of the “freezing in” of the ion contribution to the mass density along the flux tube as the current sheets and standing wave structures broaden. The normal component of the magnetic field is about  $5\text{ nT}$  (but varies with a dip down to  $\sim 0\text{ nT}$ ). This is larger than the limits on the normal component of the magnetic field observed closer to the x line which were  $\sim 1\text{ nT}$ . Thus the average normal component of the magnetic field is more intense farther from the x-line along the x-axis. This is an expected consequence of the fact that the normal component should be zero exactly at the x-line.

### 3.5.1. Evidence for Widening of the Current Sheets and Potential Structure with Distance From the x Line in the Outflow Direction

[25] In this section we provide evidence from the thin current sheet crossings at 0946:50 UT that the current sheet thickness and the electric potential structure broaden with distance away the x-line. Spacecraft 3 encounters the current sheet at a position  $2000\text{ km}$  earthward of Spacecraft 4 along the x-axis. This suggests that Spacecraft 3 is displaced  $\sim 2\text{ } c/\omega_{pi}$  in the earthward outflow direction. Figure 3b presents  $25\text{ s}$  of data from Spacecraft 3 in the same format as the  $6\text{ s}$  of data from Spacecraft 4 in Figure 3a. The data from Spacecraft 3 shows that the

distance between the bifurcated currents sheet is broader ( $\sim 1000\text{ km}$ ) than at the position Spacecraft 4. Similarly, the spatial scales of the potential well, the diamagnetic cavity and the Hall magnetic field perturbation are broader at the position of this spacecraft by a factor of 4–5. The normal component of the electric field is  $\sim 10\text{--}40\text{ mV/m}$ , and the cross current sheet potential about  $6\text{--}10\text{ kV}$ . Thus the width of the potential well along the normal ( $z$ ) direction has broadened from about  $200\text{ km}$  at the position of spacecraft 4 to about  $1000\text{ km}$  over a distance  $2000\text{ km}$  down stream in the  $x$  direction. For explicit comparison, the spatial scales and broadening of the potential structure are illustrated in Figure 4. To our knowledge, these measurements are the first explicit experimental demonstration in a space plasma of the diverging geometry of the reconnection standing waves and their related structures. These measurements provide evidence that Spacecraft 4 is very close to the electron diffusion region. It is not possible with these measurements to distinguish between the singular x-line structure of Petschek and the long thin electron diffusion region proposed on the basis of recent hybrid and PIC simulations [Biskamp, 2000; Shay et al., 1998; Shay et al., 2001; Hesse et al., 1998] and the early analytic work by Syrovatskii [1971]. We do note that the width of this current sheet is comparable to the widths ( $0.1$  ion inertial lengths) of the very thin current sheet studied in recent PIC simulations [Zeiler et al., 2002; Ricci et al., 2002]. The normal component of the electric field and the estimated  $x$  and  $y$  components of the  $\mathbf{E} \times \mathbf{B}$  velocity are also consistent with the large values found near the diffusion region in these PIC simulations. The experimental value of the normal component of the electric field as shown in Figure 12 is about  $10\text{ } V_{AH+}B_x$  or  $30\text{ } V_{AO+}B_x$  or  $0.25\text{ } V_{AcB_x}$ . The

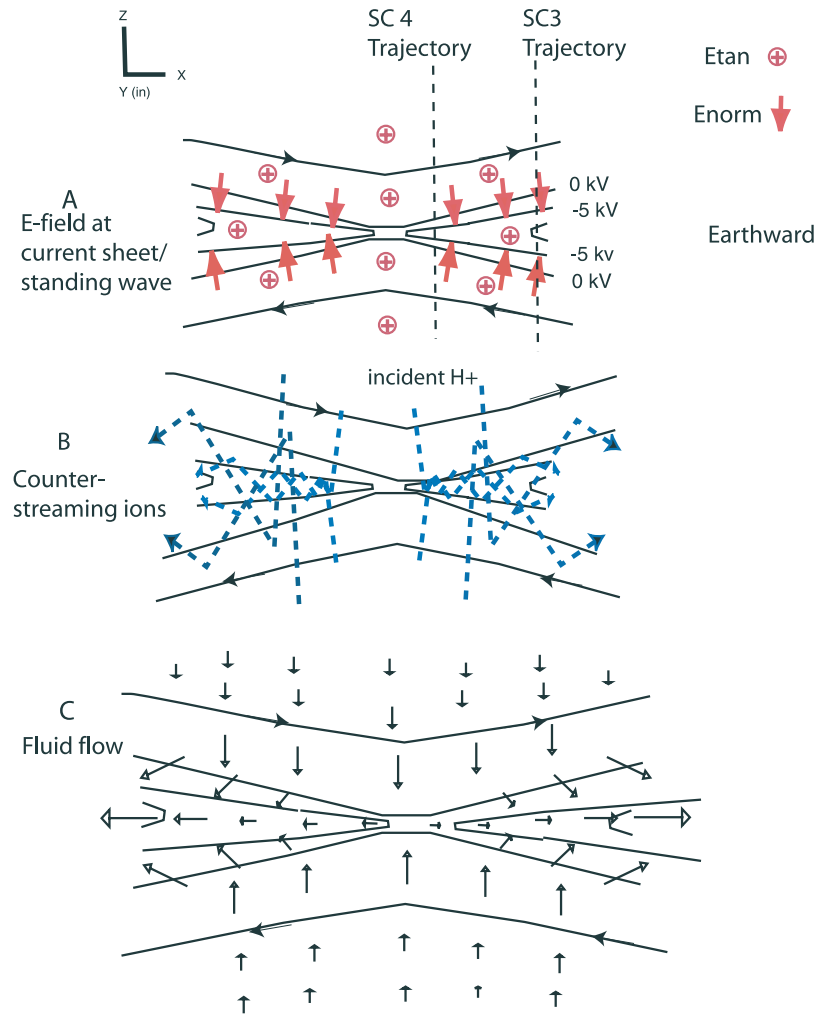


**Figure 5.** (a) Schematic of strong normal component of the electric field coinciding with standing wave/current layer near x-line. (b) Trajectory of representative ions ballistically accelerated into  $\sim 4$ – $6$  kV potential well forming quasi-trapped counter streaming beams. Counterstreaming beams produce effective pressure; deceleration of ion fluid across potential drop; and jet at  $\sim 1V_A$  along outflow direction. (c) Schematic of ion fluid flow vectors consistent with averaging over single particle trajectories.

experimentally estimated  $x$  and  $y$  components  $\mathbf{E} \times \mathbf{B}$  velocities are 6000 to 10,000 km/s or about  $0.2 V_{Ae}$ . These large  $\mathbf{E} \times \mathbf{B}$  velocities are consistent with those presented near the x-line in the simulations of Zeiler *et al.* [2002] and Ricci *et al.* [2002]. The observations of the thin current sheet, the large normal component of the electric fields, and the large  $\mathbf{E} \times \mathbf{B}$  velocity all argue for the close proximity of these observations to the x-line.

### 3.6. Evidence for Ion Beams Accelerated by the Potential Drops

[26] In principle, an upstream hydrogen ion incident with a velocity of  $>100$  km/s for  $B \sim 10$  nT would have a convected gyroradius comparable or larger than the scale size (100 km) of the potential structure and current sheet observed by Spacecraft 4. Its first adiabatic invariant would be violated and it would be accelerated across the potential structure. The potential drop is large compared to the thermal energy of the ions and therefore the accelerated

ion fluid could form a strongly monoenergetic beam with an energy comparable to the potential drop. Once inside the diamagnetic cavity the gyroradius is on the order 10,000 km since the ion has a larger velocity ( $\sim 1000$  km) due to the acceleration, and the magnetic field is weaker ( $\sim 1$  nT). The bounce time of such an ion in the potential well would be on the order of 0.1 s, which is much smaller than the gyroperiod of about 7 s in a 10 nT magnetic field. On these timescales, it is expected that such a beam could, in principle, bounce many times before the candidate electromagnetic instabilities that could disrupt it [Gary *et al.*, 1993] have time to grow. In this section, we address the experimental evidence for the acceleration of incident ions across into the potential well and the formation of the counterstreaming beam.

[27] As illustrated in Figure 5, and discussed more completely in the discussion section, the sense of each electric field pulse is such that it is directed from the tail lobe into the plasma sheet. This is the direction expected for



acceleration of positive ions into the plasma sheet and trapping them once inside. Figure 6 presents velocity space distribution functions of  $H^+$  ions from the Cluster CIS CODIF instrument at 0946:46.8 in the  $V_{ygse}-V_{zgse}$  plane (top) and the  $V_{ygse}-V_{zgse}$  plane (top). The boundary normal for the current sheet, which lies almost entirely in the  $y$ - $z$  GSE plane, is shown in the second part as a solid line through the origin. Note in the  $V_{ygse}-V_{zgse}$  distribution function, there are two counterstreaming ion beams with velocities of about  $10^3$  km/s. These velocities are symmetric about the origin and directed within 20 degrees the normal direction. The beams are strikingly monoenergetic with thermal spreads much smaller than their bulk velocities. The distributions are consistent with acceleration of one beam through the potential drop associated with the southern hemisphere thin current sheet and the other through the potential drop of the northern hemisphere thin current layer. Each beam is distorted into an arc about the velocity space origin in a manner consistent with deflection of the beam by the  $\mathbf{V} \times \mathbf{B}$  force of the magnetic field in a positive  $B_x$  field. The thermal width of each beam as indicated by Figure 6 and defined by the decrease in the count rate by a factor of  $e^{-1}$  is about 100 km/s. This suggests an extremely monoenergetic beam directed along the normal with an energy similar to that of the cross current sheet potential drop.

[28] Figure 7 displays a sequence of cuts through  $H^+$  phase space distributions covering an angular field of view of  $\sim 22$  degrees about the  $V_y$ - $V_z$  gse plane. The color scale covers four orders of magnitude. These distributions are arrayed as a function of estimated distance from the current reversal starting from the northern outer periphery of the current sheet at the top to south of the small-scale current sheet at the bottom. Figure 2 displays the trajectory of Spacecraft 1 and 4 through the current sheet. It also displays the location, times, and local magnetic field strength at the times when the distribution functions were obtained. The first three distribution functions were from Spacecraft 1, which skimmed the outer boundary of the larger scale current sheet about 1000–2000 km northward and dawnward of the thin current sheet. In this sense, Spacecraft 1 may almost be regarded as an upstream monitor. However, it should be noted Spacecraft 1 is not directly upstream of Spacecraft 4 since it is  $\sim 2000$  km earthward of Spacecraft 4. During this time Spacecraft 1 observed magnetic field magnitudes of +25 nT to 17 nT. The phase space distributions show acceleration of a cold  $H^+$  beam toward the current midplane with velocities increasing from  $\sim 100$  km/s to  $-250$  km/s. Since the large-scale current sheet has a much larger scale than the gyroradii of the beams, the motion of the  $H^+$  beams is due to  $\mathbf{E} \times \mathbf{B}$  electric field. Spacecraft 4 actually passed through the small-scale current sheet. It observes  $H^+$  beams which further accelerate toward the small-scale current sheet with velocities up to 500 km. At the outer boundary of the thin current sheet potential well, the ions beams are more oriented along the normal direction and have velocities of  $\sim 400$ –500 km/s. The beams thermal spread increase as the velocity of the beam increases. Inside the potential well and between the separatrices of the small-scale current sheet, the ions have accelerated up to  $\geq 1000$  km/s. The dominant force on the  $H^+$  ions is due to the electrostatic field and it plays a major role in the confinement of the ions. There is also evidence that a

fraction of the countering-stream beams leaks outside the potential well into the upstream region since northward directed beams are present in the northern current sheet and southward directed beams are present southward of the current sheet. This suggests that a small portion of the ion confinement to the center of the current sheet may be magnetic and due to the Lorentz force (magnetic gyration), or perhaps due to the large-scale ( $O^+$  scale) potential well surrounding the small-scale potential well.

### 3.6.1. Evidence for $O^+$ Acceleration at Large-Scale Current Sheet Potential Drop

[29] Thus far, this paper has focused on measurements of the small-scale current sheet and electric field structure near the center of the magnetic field reversal region. The magnetic field data in Figure 1 indicates that this small-scale current sheet is imbedded in a much larger-scale current sheet ( $\sim 2000$  km). The data indicates that the larger-scale current sheets have large normal components of the electric field (5–20 mV/m).  $O^+$  distribution functions provide evidence that the  $O^+$  ions, which have very large gyroradii, are accelerated by the large-scale potential structure, producing  $\sim 20$  keV counterstreaming ion structures through out the large-scale current sheet. The data indicates that these counterstreaming  $O^+$  beams are preferentially oriented along the normal direction.

[30] We emphasize that  $H^+$  ions have gyroradii which are a fraction of the scale size of this structure, so they are not ballistically accelerated, but instead  $\mathbf{E} \times \mathbf{B}$  drift toward the small-scale potential drop near the magnetic field reversal. An illustration of this multiscale acceleration scenario is provided in the discussion section with particle trajectories and potential contours shown in Figure 14.

[31] Figure 8 presents 25 s of  $O^+$  phase space distributions and fields data from the large-scale current sheet crossing that was first presented in Figure 1. Figure 8 (top) shows the estimated normal component of the electric field as provided by the measurement of  $E_{ygse}$ . The lower part presents an estimate of the electric potential drop from the spatial integration of  $E_{ygse}$  along the trajectory of the spacecraft. The velocity scale on the distribution function plots range between  $\pm 700$  km/s. Figure 8a consists of cuts through the distribution function in the  $v_{ygse}-v_{xgse}$  GSE plane; Figure 8b consists of cuts through the  $v_{zgse}-v_{xgse}$  plane; and Figure 8c consists of cuts through the  $v_{zgse}-v_{ygse}$  GSE plane. The sequence of distribution functions in the  $v_{ygse}-v_{zgse}$  plane (Figure 8c) shows a pair of counterstreaming  $O^+$  beams. The beams are largely confined to the second and fourth quadrants consistent with orientation along the normal direction. The beams have velocities  $\sim 400$ –500 km/s and energies of 15–25 keV. The  $O^+$  beams are present over a much broader spatial scale than the  $H^+$  beams presented earlier. Because the  $O^+$  beams are found over a large fraction of the large-scale ( $\sim 2000$  km) current sheet, they could not have been accelerated by the small-scale (4–6 keV) potential well which was encountered over a period of  $\sim 3$  s or a distance along the normal of  $\sim 200$ . For this reason, we investigate the electric field structure of the large-scale current sheet.

[32] As shown in Figure 1, the value of  $B_{xgse}$  increases from 12 nT to 25 nT during the traversal of the northern portion of the large-scale current sheet over a period of about 20–30 s. This timescale corresponds to a distance

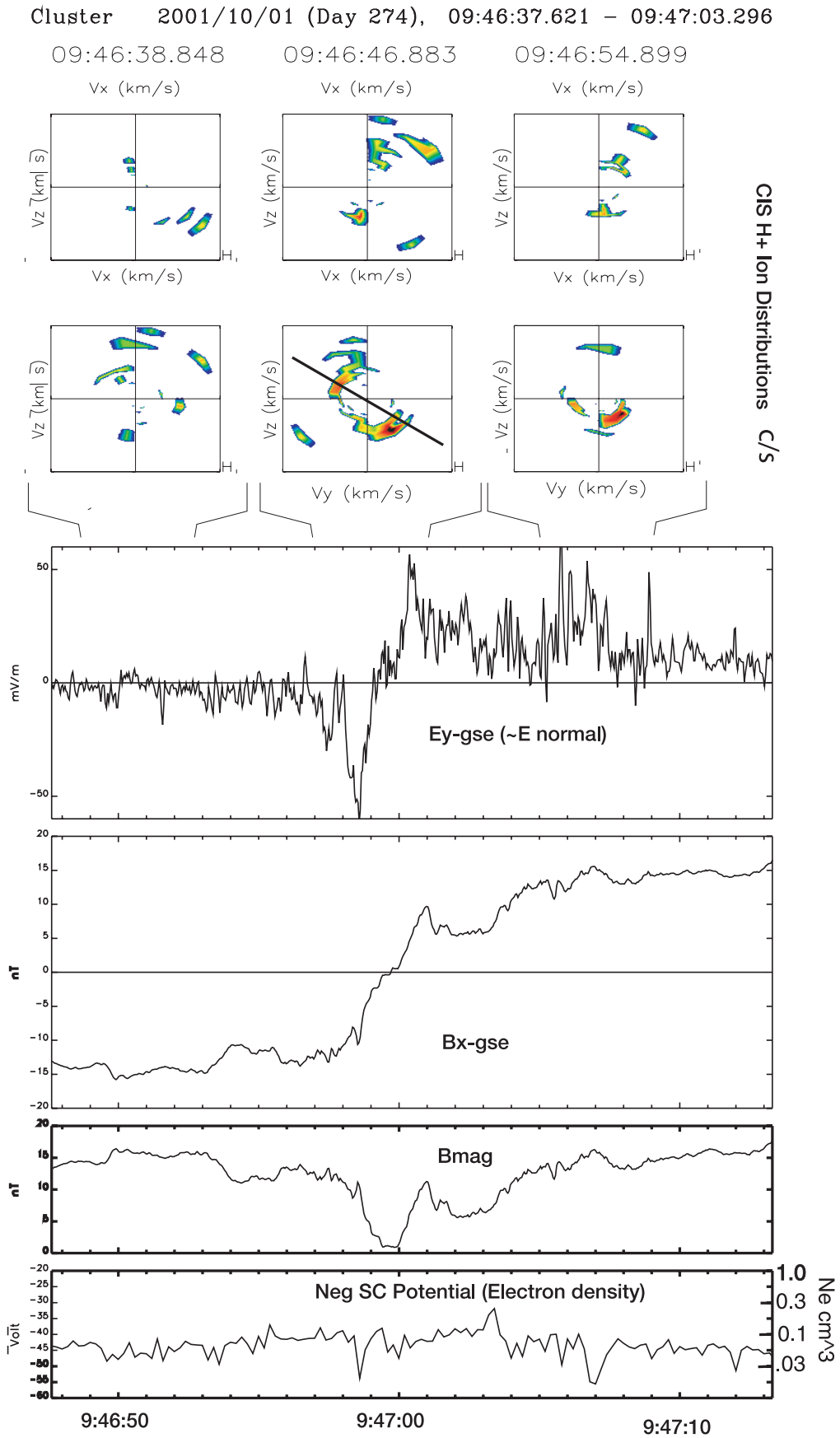


Figure 6

October 1, 2001  
CIS-CODIF

Southward beam accelerating  
towards mid-plane

Counter-streaming  
ion beams  
~oriented along normal

Northward Beam  
towards mid-plane

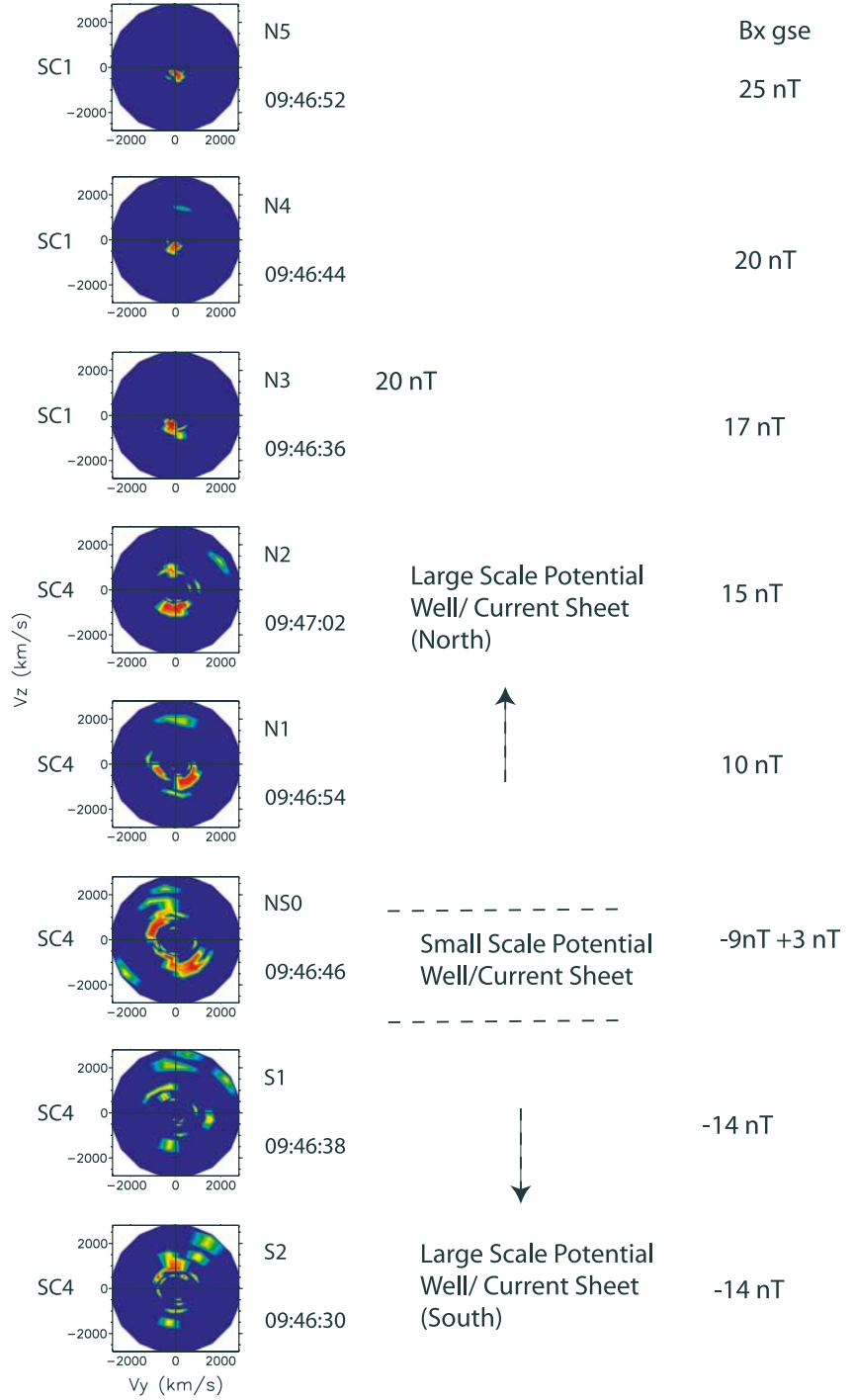


**Figure 7.** Spacecraft 1 and Spacecraft 4  $H^+$  phase space distributions in  $V_{ygse}$ – $V_{zgse}$  plane on 1 October 2001 from 0946:30 to 0946:52 UT. Distribution functions are arrayed in distance from magnetic field reversal/small-scale potential drop. Color scale ranges over four orders of magnitude. Value  $B_{x\text{gse}}$  listed at time of particle measurements.

**Figure 6.** CIS  $H^+$  distribution function (4 s every 8 s) showing spatial evolution of counter streaming ion beam structure through current sheet electric field structure. (top)  $H^+$  counts/s color coded in  $V_{zgse}$ – $V_{ygse}$  plane, (bottom)  $H^+$  counts/s color coded in  $V_{zgse}$ – $V_{ygse}$  plane. Velocity range of ion plots  $\pm 2800$  km/s. Middle plot in bottom row shows counter-streaming ion beam at  $\sim 1000$  km/s oriented approximately along normal (solid line). First line plot is  $E_{ygse}$  which is dominated by E-normal,  $B_{xgse}$  showing current layer, magnitude of magnetic field, negative spacecraft potential in volts as an estimate of electron density.

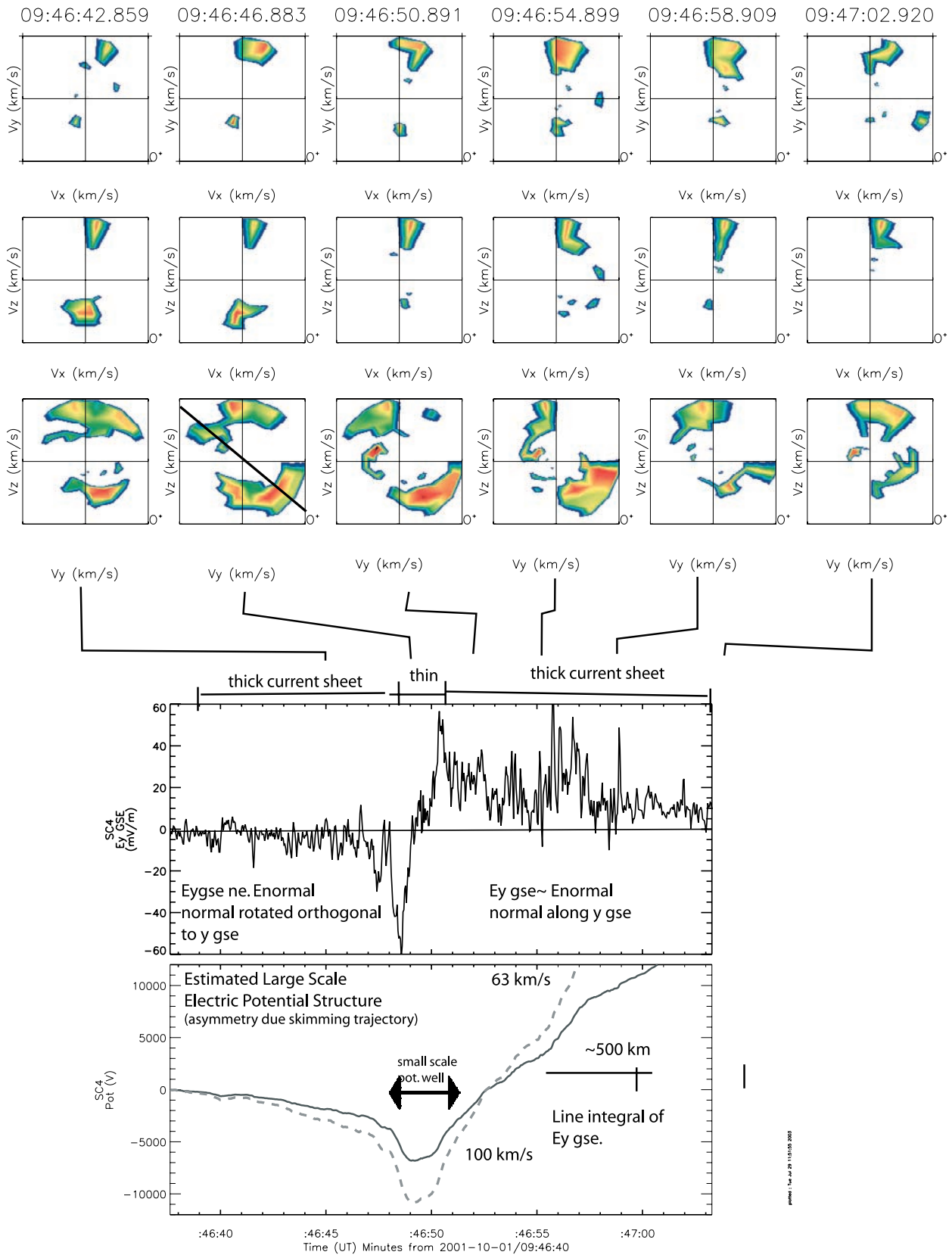


**Figure 8.** CIS O<sup>+</sup> velocity space distributions (4 s) in counts/s in same format as Figure 3 for the same time interval. Data shows counter streaming O<sup>+</sup> beams over broader spatial scales coinciding with large scale potential well. Electric field data shows asymmetric potential well over large scales (see text which argues asymmetry is an artifact of the rotation of the current sheet normal out of the two-dimensional plane of the electric field measurements as the spacecraft skims through the large-scale current sheet structure).



along the normal of about 2000–3000 km. This is also consistent with measurements of  $B_{xgse}$  by Spacecraft 1 and 4 which indicate both were in the northern portion of the current sheet simultaneously. Figure 1 indicates that  $E_{ygse}$  (Figure 8d), which is in the approximate normal direction, ranges between 5 and 15 mV/m. Thus there is evidence of a larger-scale electric field structure along the normal direction which coincides with the large-scale current sheet. A rough estimate of the potential drop across this current sheet (Figure 8e), provided by the spatial integration of  $E_{ygse}$ , is  $\sim 30$  kV. This potential drop is comparable to the energy of the  $O^+$  ion beams. Only an approximate value of the potential can be obtained because the electric is measured only in the x-y GSE plane. A second feature of the measurement is that the trajectory of the spacecraft is a skimming trajectory through the current structure. One consequence of the skimming trajectory of Spacecraft 4 is that it traverses a large portion of the northern large-scale current sheet but only a fraction of the southern current sheet. For example, the maximum  $B_{xgse}$  value encountered during the northern current sheet is  $\sim 30$  nT while the minimum encountered during the southern current sheet is only  $-15$  nT. This asymmetric encounter with the current sheet provides one explanation for the apparently asymmetric potential structure in Figure 8e. To overcome the limitations of the single crossings, we investigate at an individual and statistical level a number of crossings observed over the 0940 to 0955 time frame. These current sheet crossings cumulatively span the current sheet.

[33] A second effect on the accuracy of the potential estimate is that the current sheet normal direction gradually rotates due to the 100 s large-scale MHD wave. Near the magnetic field reversal, the normal is within about 30 degrees of the y GSE direction and 50 s later, due to the motion of the wave, the direction of the normal has rotated so that it is approximately along the z GSE direction. At this position the contribution to the line integral of  $E_{ygse}$  is not due to a displacement along the normal direction and may also not be due to the normal component of the electric field. For this reason, we should only consider the line integral between  $\pm 20$  seconds of the magnetic field reversal in our discussion of the large-scale potential well.

[34] There is another effect which produces an asymmetry in the potential structure between the northern and southern current sheets. If the normal component of the electric field is antisymmetric across the current sheet and there exists a constant tangential component of the electric field, vector addition of the two components results in a rotation of the direction of the total vector away from the normal direction. Figure 11b illustrates this effect for a current sheet with a normal direction similar to that of the crossing we have studied. In this example, the tangential component ( $E_{tan}$  in figure) is about 0.5 of the normal component ( $E_{norm}$ ), and it rotates the total electric field vector ( $E_{tot}$ ) by about 30 degrees. The rotation is in the opposite direction in the northern and southern current sheet. In the northern current sheet, the total electric field vector is rotated into the measurement plane producing a strong measured  $E_{ygse}$  component which is roughly comparable to the original normal component. In the southern current sheet, the total electric field vector is rotated away from the measurement plane resulting in a smaller measured  $E_{ygse}$ . This rotation

is probably the dominant effect in producing the asymmetric electric field structure.

[35] The z gse component of the electric field, which is not measured by the electric field instrument, may sometimes be estimated from the MHD assumption that  $\mathbf{E} \cdot \mathbf{B} = 0$  thereby providing all three components of the electric field vector. In cases similar to our situation in which the ambient magnetic field vector is directed nearly orthogonal to the direction of the unknown electric field component, the error propagation effects are particularly severe and the estimate is especially inaccurate. For this reason, we have not used the  $\mathbf{E} \cdot \mathbf{B} = 0$  approximation to estimate the spin axis (z GSE) component of the electric field.

[36] Owing to these measurement uncertainties, it is difficult to accurately determine the electric potential drop along a path normal to the current sheet. We can roughly estimate the large potential drop from the following considerations: (1) the normal component of the electric field dominates over the tangential component of the electric field over most of the large-scale current sheet; (2) the normal component is direction is toward the magnetic field reversal; (3) the normal component of the electric has a magnitude of roughly 10 mV/m over an appreciable portion of the current sheet; (4) this value of the normal component dominates over contributions due to Lorentz transformation of the data from the spacecraft frame into the rest frame of the wave; and (5) the scale size of the current sheet is 2000–3000 km. The typical potential drop across the large-scale current sheet is estimated to be 15–30 keV. It is quite possible that the value for an individual crossing may larger. This estimated potential drop and the associated potential well is deeper than that associated with the small-scale current sheet and is consistent with the energy of the counterstreaming  $O^+$  beams. These estimates highlight the importance of three-dimensional measurements of the electric field by multiple spacecraft. They also suggest the importance of detailed modeling of the wavy current sheet potential structure using conformal mapping techniques incorporating the two-dimensional (2-D) electric field data from the four spacecraft. Finally, they suggest the importance of large-scale 3-D particle in cell or hybrid simulations. These more sophisticated analyses are likely to provide important insights into the kinetic interaction of ions with the waves, which are not present in this preliminary analysis.

### 3.6.2. Statistical Evidence for 15–30 kV Potential Drop Across Large-Scale Current Sheet

[37] In this section, about 30 individual current sheet crossings are surveyed to assess the electric field structure of the large-scale current sheet. Figure 9 presents measurements of  $B_{xgse}$  (black trace) and  $E_{ygse}$  from Cluster spacecraft 1 (top), spacecraft 3 (middle), and spacecraft 4 (bottom) over the time interval from 0940 UT to 0955 UT. Both quantities are averaged over the 4-s spin period of the spacecraft and therefore present a large-scale view of the current sheet fields. The  $B_{xgse}$  component shows numerous passes from the Northern tail lobes to the southern tail lobes and back indicating a large number of encounters with the cross-tail current sheet. The largest positive  $B_{xgse}$  values observed are  $\sim 30$  nT and the most negative values of  $B_{xgse}$  are  $\sim -30$  nT. A schematic picture of the current sheet consistent with these crossings is shown at the top of

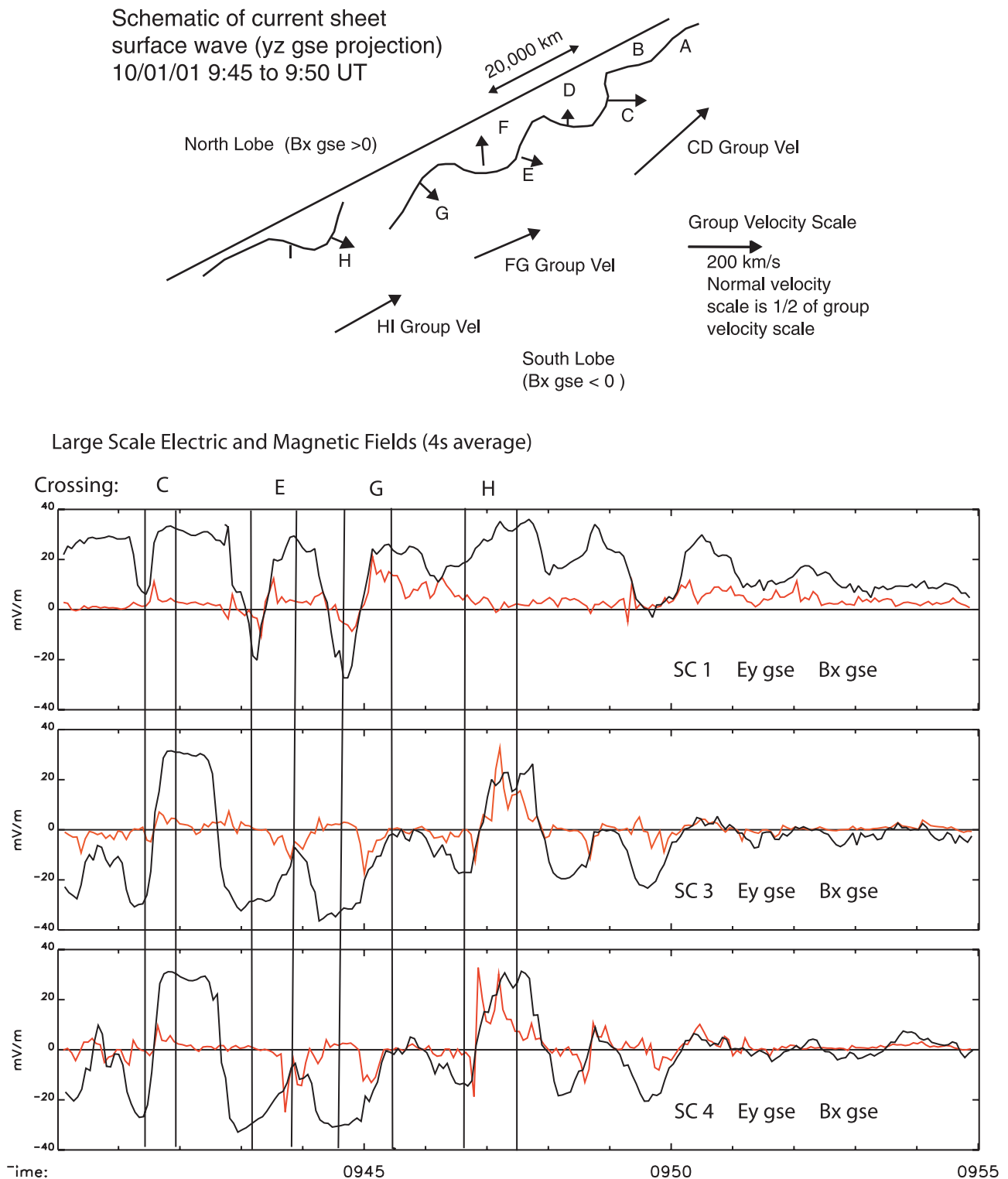


**Figure 9.** Structure of large-scale normal component of electric field. (top) The y-z GSE plane, which illustrates the rocking of the vectors associated with undulating current sheet along with the shape of a current sheet responsible for the vectors. (bottom)  $E_{y\text{gse}}$  (red) and  $B_{x\text{gse}}$  for the crossings over 0940–0955 UT. Crossings labeled C, E, G, and H correspond to South to North (negative to positive  $B_x$  GSE) current sheet transitions and correspond to crossings in which vector normal to current sheet points in  $\sim y$  GSE direction.

Figure 9. The arrows and letters denote individual passes and the direction of the current sheet normal determined from spacecraft timing. The arrows reveal the systematic rocking motion of the boundary normal as the current sheet passes over the spacecraft. Boundary normals obtained during Northern to Southern Hemisphere passes (decreases in  $B_{xgse}$ ) are directed nearly vertical (in the  $z_{gse}$  direction). Boundary normal vectors obtained during Southern to Northern Hemisphere magnetic field transitions (increases in  $B_{gse}$ ) tilt in the  $+y_{gse} - z_{gse}$  quadrant with the  $z_{gse}$  and  $y_{gse}$  components approximately equal in magnitude. During typical current sheet transitions associated with decreases in  $B_{xgse}$ , the  $E_{ygse}$  component of the electric field is small. The largest electric field values are associated with current sheets in which the  $B_{xgse}$  component increases. This provides evidence that the electric field perturbations have a strong component in the normal direction relative and a smaller component in the tangential direction. Notice that  $E_{ygse}$  is often bipolar in association with transitions from large negative to large positive  $B_{xgse}$ . The spacecraft world line often skims the current sheet, resulting in partial crossings in which only half the current sheet is traversed. These crossings are associated with negative electric field pulses which peak when  $B_{xgse}$  increases. These observations are consistent with large-scale electric field structures directed along the current sheet normal towards the center of the current sheet. Since the electric fields and the associated current sheets are observed for periods of  $\sim 30$  s, it implies that the structures are about 2000–3000 km wide. An estimate of electric potential drop along the spacecraft trajectory based on the measured electric field is  $\sim 20$ –40 kV across the current sheets. As discussed above, uncertainties associated with these estimates are largely associated with the lack of an instantaneous three-dimensional measurements and resultant ambiguities in the projection of the electric field ( $E_{ygse}$ ) along the spacecraft velocity relative to the moving structure. In this case, the velocity of the structure relative to the Earth (and spacecraft) is  $\mathbf{v}_s \sim 200$  km/s ( $0.86 \mathbf{i}_{gse} + 0.5 \mathbf{k}_{gse}$ ). As in the case of the thinner current sheets, the electric potential structure is that of a potential well with the minimum at the center of the magnetic field reversal.

[38] Figure 10 (top) presents the large-scale normal component of the electric field (red trace) and  $B_x$  GSE (black trace) across the large-scale current sheets obtained by averaging  $\sim 20$  passes of the data presented in Figure 9. The data used in the top part of Figure 10 was obtained from those passes when the vector normal to the current sheet had a large projection along the  $y_{gse}$  axis. As described previously, this includes data from those passes that were associated with increases in  $B_{xgse}$ , that is, passes from the southern portion of the current sheet to the northern portion. The averaged data from these passes shows a large-scale bipolar signature across the current sheet over a period of about 20 s or 2000 km. There is an asymmetry in the electric field with the northern hemisphere portion of the current sheet having an average value of about 12 mV/m while the southern hemisphere portion of the current sheet is about  $-7$  mV/m. The estimated potential drop is 20–30 kV. The top part of Figure 10 consists of passes in Figure 9 during which the magnetic field decrease during the pass indicating transition from northern hemisphere current layer

to southern hemisphere current layer. These passes are characterized by current sheet normal vectors, which are predominately perpendicular to the electric field measurement plane. In the limit that all normal vectors were exactly perpendicular to the measurement plane that the current sheet was two dimensional and steady state and that the measurements were obtained in the rest frame of the current sheet, we would expect that the measured component would be dominated by the tangential component of the electric field, which is likely to be constant and small. However, since the normal direction is not exactly perpendicular to the measurement plane, we can expect a contribution to  $E_{ygse}$  from the comparatively large normal component of the electric field. This contribution is approximately equal to  $E_z \sin\phi$ , where  $\phi$  is the angle between the normal to the current sheet and the  $z$  GSE direction. Since  $\phi \sim 20$ –35 degrees, the contribution to  $E_{ygse}$  from the normal component  $\sim (0.3$ – $0.5) E_{norm}$  or 4–7 mV/m. Another contribution is from the fact that the current sheet has a velocity along its normal of about 80 km/s which should produce a 1–2 mV/m jump in the tangential component of the electric field. Finally, we note the averaged data in the lower panel of Figure 10 shows a dc offset of about 5 mV/m for the bipolar structure. One source of such an offset would be the local normal incidence frame tangential component of the electric field which would be a positive constant tangential component of the electric field of  $\sim 5$  mV/m across the current layer. This field is of the correct direction to create a normal component of Poynting flux and mass flow into the reconnection structure. This evidence for the tangential component of the electric field must be regarded as circumstantial given the statistical nature of the argument and the uncertainties in the normal direction. However, this value of the tangential component of the electric field is consistent with the  $H^+$  fluid velocity immediately upstream of the small scale current sheet. The  $H^+$  fluid velocity is directed along the normal to the current sheet and is  $\sim 300$ –400 km/s. In the boundary normal system,  $B_x \sim 12$  nT  $\gg B_y$  and  $B_x \gg B_z$  we have  $E_{tan} \sim 3.5$ –5 mV/m.

[39] The fact that the electric field in the lower panel of Figure 10 is a fraction (30–50%) of that in the top part provides strong evidence that there is a bipolar electric field profile across the large-scale current sheet directed in the normal direction which is larger than the tangential component. This electric field structure produces an electric potential with an average depth of 15–30 kV well centered on the midplane of the current sheet. Individual passes through the current sheet produce potential drops as large as 40 kV. This is a large fraction of the total convection electric field across the tail which may be estimated from low-altitude measurements of the low altitude polar cap potential drop to be 80–150 kV during active periods [Reiff *et al.*, 1981; Wygant *et al.*, 1983].

### 3.7. Evidence From Amperes Law That the $\mathbf{E} \times \mathbf{B}$ Drift of the Electrons is a Major Contributor to the Current Sheet Intensity at the Thin Current Sheet

[40] The close relation between the shape of the potential drop and the shape of the diamagnetic cavity (Figure 3a, third part) is related to the dominant role of the  $(\mathbf{E} \times \mathbf{B})_y$  drift of magnetized electrons in producing the current

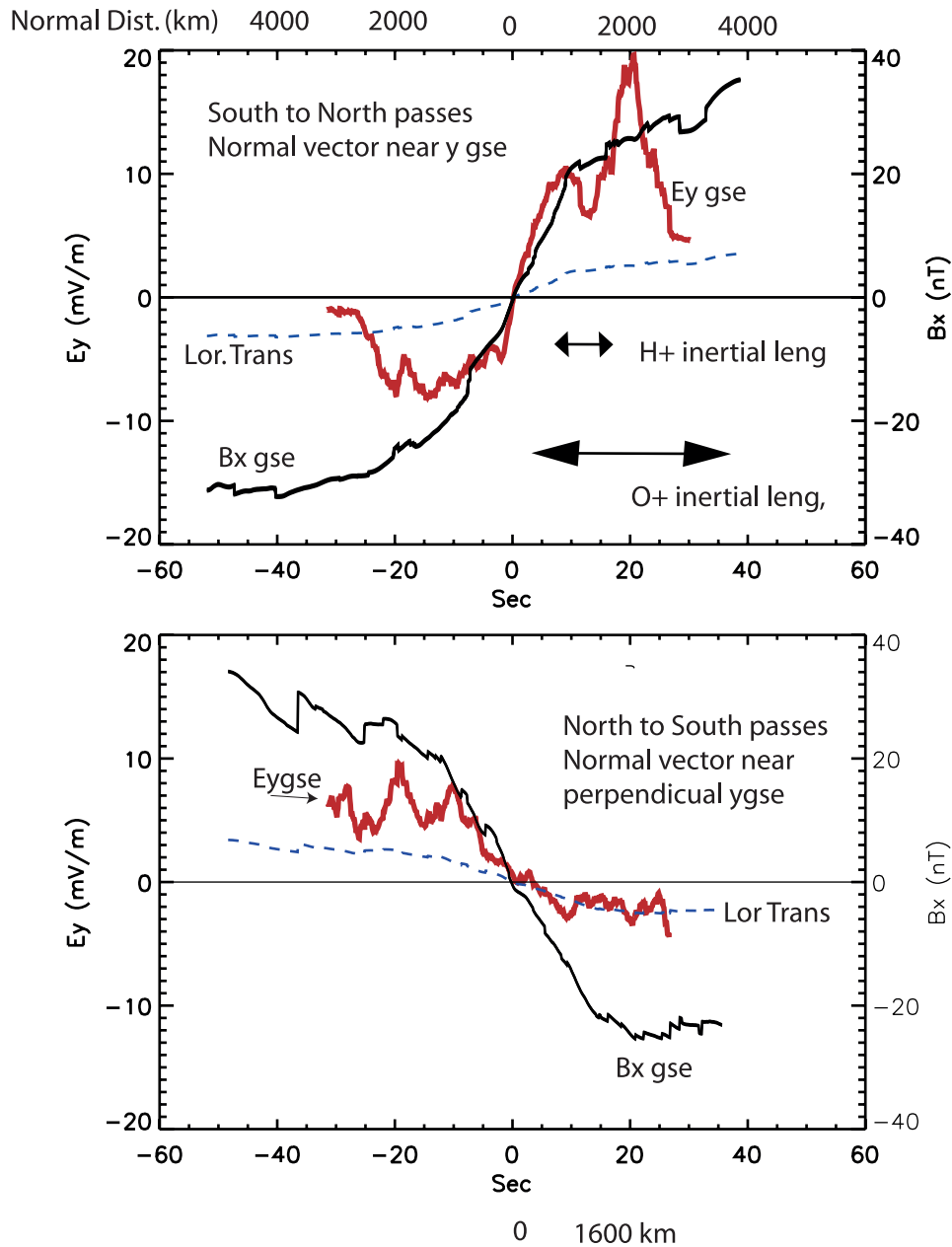


**Figure 10.** Statistical analysis illustrating the dominance of the normal component of the electric field over other contributions in the thick current sheet.  $E_{ygse}$  is presented in a frame at rest relative to the kinked current sheet structure. (top) Average  $E_{ygse}$  when it is strongly dominated by the normal component of the electric field (south current sheet to north current sheet transitions). (bottom)  $E_y$  from passes when the normal vector is more than 60 degrees from the  $E$  field measurement plane (north current sheet to south current sheet transitions).

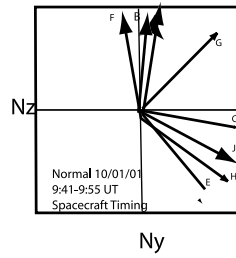
density,  $J_y$  responsible for the magnetic shear of the nearly antiparallel magnetic field lines.

[41] Figure 12 shows that the  $y$  gse component of the  $\mathbf{E} \times \mathbf{B}$  drift of the electrons peak value is  $\sim 10,000$  km/s. Assuming a constant electron density, we can integrate the current density due to the  $\mathbf{E} \times \mathbf{B}$  drift of the electrons over the observed spatial scale of the current sheet and use Amperes law to estimate the magnetic field jump  $\Delta B_x(z) \sim 4\pi e \int n(z)[E(z)/B_x(z)]dz$ . The estimated change in  $B_{xgse}$  from this integral is 20 nT which is comparable to

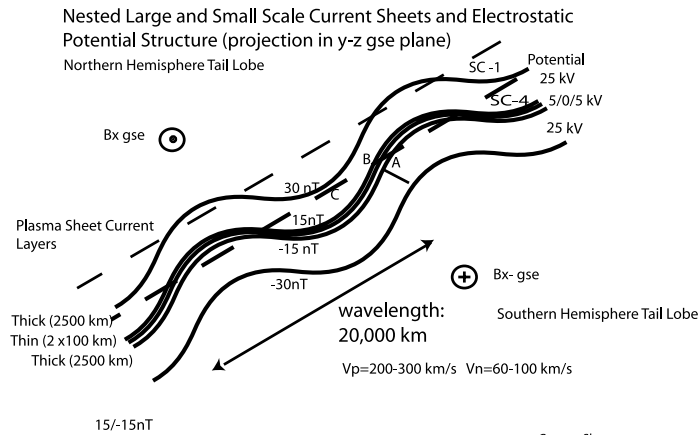
the measured change in  $B_{xgse}$  from  $-10$  nT to  $+10$  nT. This suggests that  $\mathbf{E} \times \mathbf{B}$  drift of electrons is capable of providing a large fraction of current intensity. Another contribution to the current may come from the electron pressure gradient drifts and drifts due to meandering motion in the gradients of the magnetic field reversal. We estimate the total contribution to the current density from  $\mathbf{E} \times \mathbf{B}$  drift by the electrons is 50–100%. This suggests the remaining unmeasured contribution to the current due to the electron pressure or meandering motion is on the order of 0–50%. The relatively



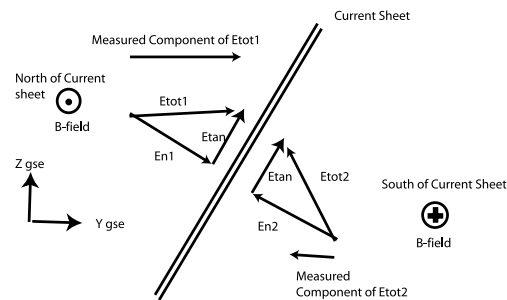
### A Normal Vector Determination



### B



### C



### D

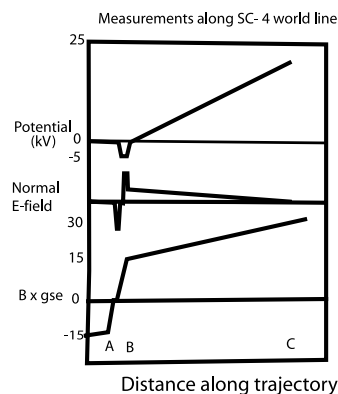


**Figure 11.** (a) Normal vectors determined from spacecraft timing. All vectors with positive  $N_z$  are North to South current sheet transitions and  $N_z$  negative South to North transitions. (b) Illustration of spacecraft 1 and 4 skimming trajectories through the large-scale current sheet. (c) The effect of the tangential component of the electric field in rotating the total Southern hemispheric electric field out of the measurement plane of the instrument. (d) Illustration of the asymmetric artifact in potential structure produced by  $E_y$  GSE integration along trajectory of spacecraft.

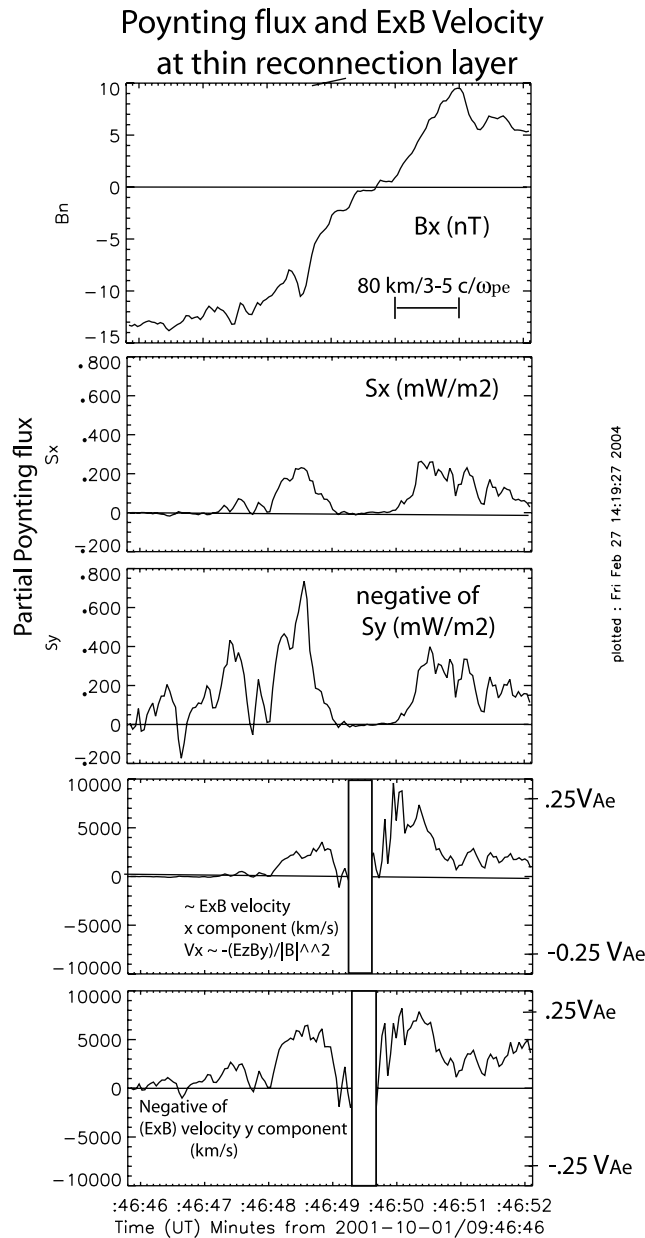


**Figure 12.** Measured  $B_x$  magnetic component; calculated Poynting flux  $x$  and  $y$  GSE components; and  $E \times B$  velocity  $x$  and  $y$  GSE components from Spacecraft 4 passage through the small scale current sheet near reconnection region. Units on right-hand side of velocity plot are relative to electron Alfvén velocity.

large uncertainties in these estimates are associated with uncertainties in the density determined from spacecraft potential. Recent PIC simulations by Zeiler *et al.* [2002] suggest equal contributions from electron pressure gradient and  $E \times B$  drifts.

[42] Figure 6 (bottom) presents an estimate of the electron density derived from the spacecraft potential (the potential difference between the surface of the spacecraft and a fixed current biased electric field probe). The (negative of the) spacecraft potential at this time was on the order of  $\sim -40$  volts and roughly constant during the

time interval of Figure 6. For a typical range of electron temperature in this region of 30 eV to 200 eV, this corresponds to a density of approximately 0.1 particles/cm. Calibrations of spacecraft potential in terms of density for the observed electron temperature range of 10–200 eV are typically accurate to about 50%. The total electron density may also be obtained (assuming quasi-neutrality) from the sum of the proton and oxygen ion number densities from the ion composition experiment. These two determinations agree and indicate the total number density is about  $0.1 \text{ cm}^{-3}$ . This value of the density indicates that the electron inertial length ( $c/\omega_{pe}$ ) is about 20 km. The width of the thin current sheet and the associated unipolar electric field pulse (100 km) is a distance of  $\sim 3\text{--}5 \text{ } c/\omega_{pe}$ . The gyroradius of a 10–200 eV electron in a 10 nT field is 1–4 km. This scale is much smaller than the width of the electric field pulse. In the absence of other fields, the electrons are therefore magnetized and  $E \times B$  drift over most of the spatial extent of the electric field pulse.

[43] As argued in the Introduction and in more detail in the discussion section, the dominance of the contribution to the current intensity of the electron  $E \times B$  drift over electron pressure gradient drifts, and ion drifts allows the estimate that the electrostatic potential drop is given by  $e\phi \sim B_x^2/8\pi n_e$ . Figure 13 presents a comparison of these two quantities that argues for their rough equality under these special circumstances. The deviation from equality of these two quantities in the last seconds of the plot may be the consequence of the fact that the spacecraft displacement through the current sheet reverses direction along the normal and is moving back towards the center for the current sheet. This is supported by Figure 12 which shows that for most of the plot  $B_x$  increases from negative to positive values indicating passage across the current sheet from North to South but then  $B_x$  reaches a maximum and for a period begins to decrease, consistent with motion back toward the center of the current sheet. This reversal in Spacecraft world line could be due to a small scale warping of the current sheet.

[44] Uncertainties in the contributions of electron  $E \times B$  drift to the current sheet intensity estimate are largely due to the  $\sim 50\%$  uncertainties in the calibration of spacecraft potential as density. Although electron pressure gradients could also provide drifts, there is no convincing evidence for enhanced electron density between the separatrices, which would be evidence for strong electron pressure gradient at thin current sheet crossing. This crossing, which is unusual compared to the other crossings obtained during 0940–0950 UT because of its very strong bipolar electric field structure and its small scale current sheet structure, is also unusual because the spacecraft potential is not systematically enhanced between the current sheets. The lack of a systematic increase in the spacecraft potential stands in strong contrast to the strong dip in the magnitude of the magnetic field. The magnitude of the magnetic field decreases from  $>10$  nT outside the current layer to about 1 nT within. Assuming total particle and magnetic pressure balance across the current layers, this implies a plasma beta of  $>100$  between the current layers. As we shall discuss, this scenario suggests that a large portion of the particle pressure is due to the

plotted : Fri Feb 27 14:19:27 2004

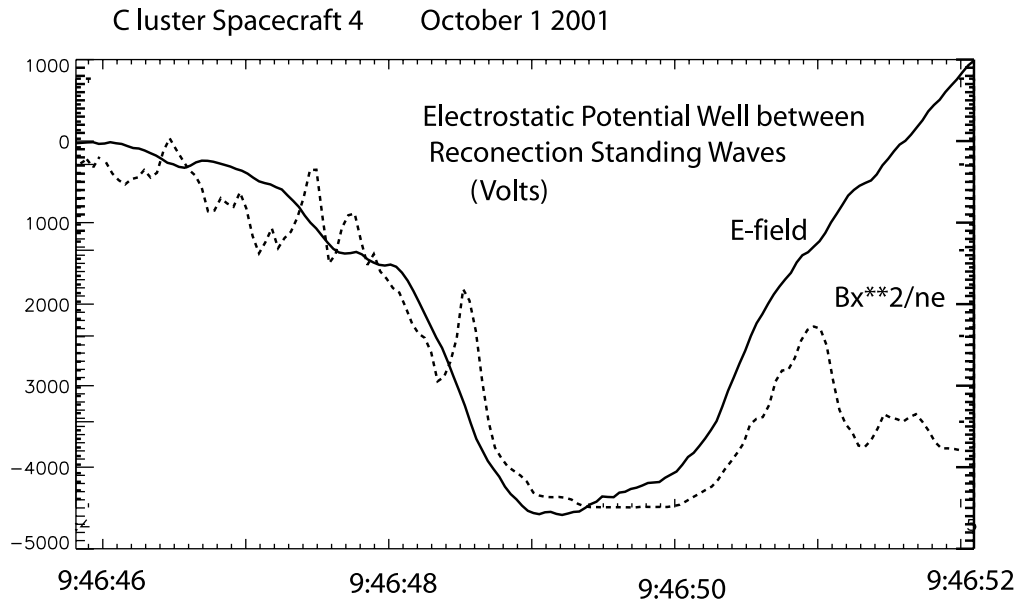


**Figure 13.** Comparison of electrostatic potential drop to quantity  $B_x^2/8\pi ne$  at thin current sheet.

counterstreaming ions which have been accelerated into the potential well.

#### 4. Discussion

[45] In this paper, we focused on a series of tail current sheet crossings during a major geomagnetic storm on 1 October 2001 when Cluster was near local midnight near the equatorial plane. During this time ion flow data shows that ion flow was first tail ward for a period of  $\sim 15$  minutes, followed by a period of fluctuating flows, and then steady earthward flow. The flows were several hundred to  $\sim 1000$  km/s. A similar pattern was observed for the estimated Poynting flux. The ion flows are roughly in the range of the Alfvén velocity and the interpretation of the events are consistent with the classical picture [Hones, 1979] of the tailward passage of the reconnection region over the spacecraft. During this time interval, the four Cluster spacecraft observed large-amplitude fluctuations in the plasma sheet current layer. The 10-min interval occurs during the peak of a major geomagnetic storm, in the near-Earth plasma, near local midnight, at the magnetic field reversal where and when rapid magnetic energy release is believed to occur. The observations and analysis by Runov *et al.* [2003b], during the interval just after the 0946:46 UT crossing presented herein, show that changes direction of magnetic curvature determined from the four Cluster spacecraft coincide with changes with the direction of plasma jetting.

##### 4.1. Statistics of Large-Scale Bipolar Normal Electric Field Structure

[46] The total number of current sheet encounters by the Cluster spacecraft was cumulatively about 40. Of these, about 10 were monitored by spacecraft 2 which samples the electric field data through an analog channel with no antialiasing filters and was therefore not included in the final data set. Owing to the rocking motion of the normal associated with the passage of the current sheet kinks, approximately one-half of the normal vectors observed were

within  $\sim 35$  degrees of the  $y$  GSE axis. Under these circumstances, the measured  $E_{y_{gse}}$  is strongly dominated by the normal component of the electric field with smaller contributions from the tangential component. Approximately seven crossings could be characterized as nearly complete passages through the current sheet with  $B_{x_{gse}}$  varying from  $-20$  nT to  $+20$  nT, while the remainder encountered only a part of the current sheet along “skimming trajectories.” These partial crossings were associated with magnetic field changes of  $-20$  nT to  $0$  nT or  $0$  nT to  $20$  nT. Five of the seven nearly complete crossings were associated with bipolar signatures in the electric field. Of the partial passes through the current sheet, the  $\sim 0$  to  $20$  nT transitions observed positive electric field pulses, while the  $-20$  nT to  $\sim 0$  nT transitions observed negative electric field pulses. Thus the data from partial crossings provides support for the existence of an average large-scale bipolar normal component of the electric field on the order of about  $\pm 10$ – $20$  mV/m over distances of  $2000$ – $3000$  km. The resultant potential drops are  $20$  to  $40$  kV, a substantial fraction of the large scale potential drop across the magnetosphere which typically ranges between  $100$  and  $150$  kV during active periods.

##### 4.2. Statistics of Passes With Subion Inertial Scale Bipolar Electric Field Structures and Associated Potential Wells

[47] A significant fraction of the current sheets have scale sizes which are on the order of or smaller than the hydrogen inertial length,  $c/\omega_H^+ \sim 700$  km or less. The smallest scale size current sheet, at 0946:47 UT, was significantly smaller than the hydrogen inertial length and its half width was on the order of  $3 c/\omega_{pe} \sim 100$  km at the position of spacecraft 4. The existence of these small-scale current sheets as well as clear Hall magnetic field signatures suggests that not only did the spacecraft encounter the reconnection region but that many of the crossings were within  $4 c/\omega_H^+$  of the reconnection  $x$ -line in the  $x$  direction. For example, simulations by Shay *et al.* [1998] show that the width of the current layers scales with distance from the  $X$  line and that current

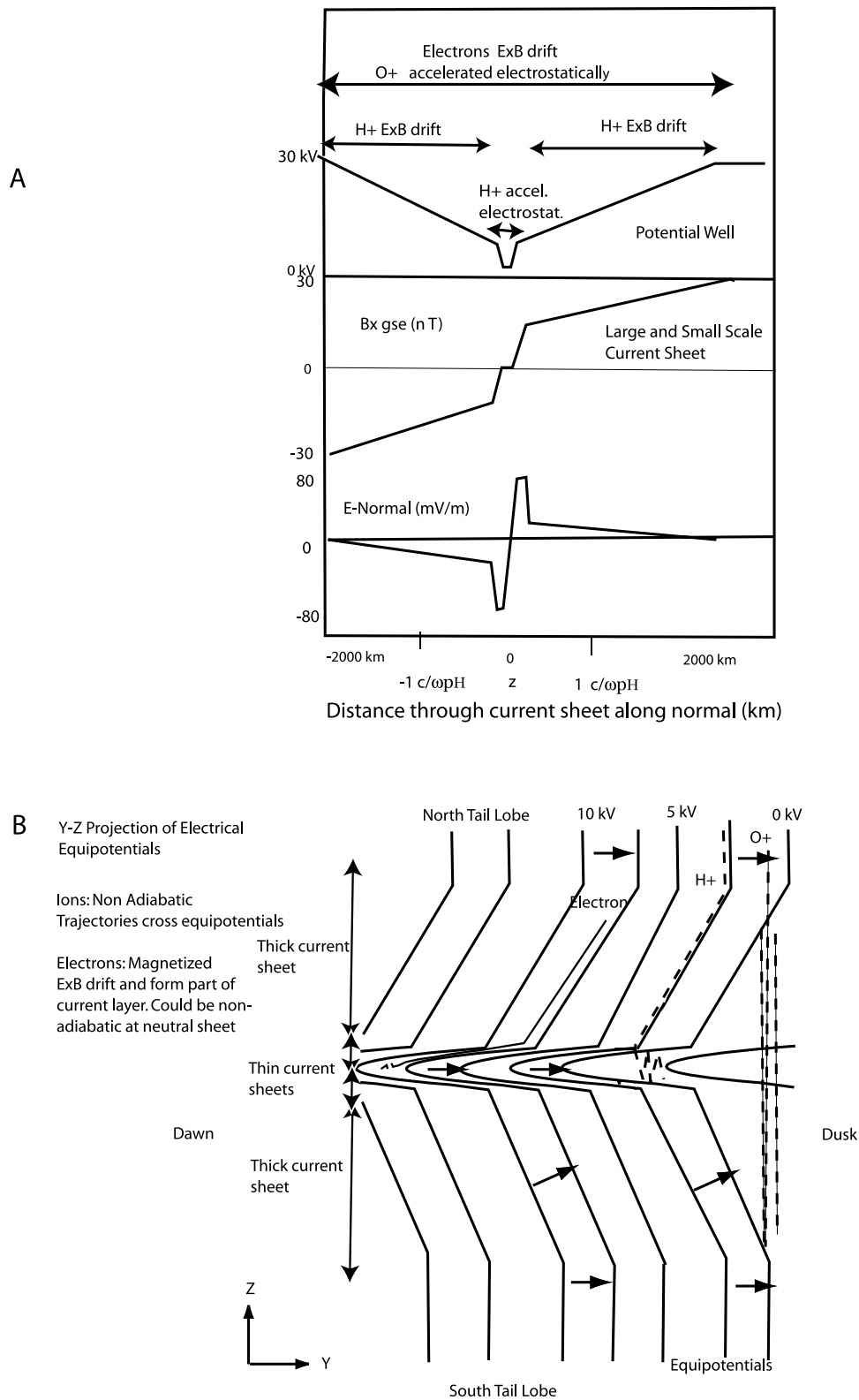


**Figure 14.** (a) The electric field, potential, potential, and magnetic field  $B_x$  GSE structure observed by a hypothetical spacecraft moving along the normal direction through current sheet near x-line. (b) Equipotential contours of potential well (solid lines) and representative particle trajectories (dotted lines) projected into y-z plane. Here  $z$  is locally normal to current sheet and  $y$  is tangential and along the current layer (out of plane). Arrows are the electric field vectors.



sheets with widths on the order of the ion inertial length are within  $4 c/\omega_{H^+}$  of the X-line. This paper focused the sub-ion inertial length current sheet crossing observed at 0946:47 UT by Spacecraft 4 and the same crossing as observed at a distance of  $3 c/\omega_{Pe}$  downstream of Spacecraft 4 in the outflow region by Spacecraft 1.

[48] A comparison to simulation scales in hybrid simulations by Shay et al. and to particle in cell simulations by Rogers suggests that Spacecraft 4 was within  $1 c/\omega_{H^+}$  of the x-line on the basis of the current sheet width. The observations by Spacecraft 4 also show that ion beams directed in the outflow direction were well below the Alfvén velocity, indicating that Spacecraft 4 was sufficiently close to the x-line that the ions had not yet accelerated up to the expected Walén condition velocity.

### 4.3. Conceptual Picture for Generating the Normal Component of the Electric Field

[49] A conceptual and simplified picture of the origin of the normal component of the electric field may be obtained by considering the Lorentz force on the electron current layer and how it couples through the normal component of the electric field to the ions. We ignore many complications in this picture and assume the structure is steady state, two-dimensional globally, and one-dimensional locally. The force on the electron fluid in the  $z$  direction is given by

$$nm_e dV_{ez}/dt = (\mathbf{j}_e \times \mathbf{B})_z/c - neE_z - \partial p_e/\partial z, \quad (1)$$

where  $V_{ez}$  is the  $z$  component of the electron fluid,  $\mathbf{j}_e$  is the electron current ( $ne\mathbf{V}_e$ ),  $n$  is the total electron number density, and  $E_z$  is the normal component of the electric field. For this conceptual picture, we assume the electrons are cold and the electron pressure gradients are dominated by the electric field. This approximation is sometimes violated [see, for example, *Mozer et al.*, 2003] but the data presented during the 0946:47 crossing (Figure 3) suggests that it holds for the thin current sheet crossing. The electron fluid in the electron current layer is accelerated towards the midplane by the net force acting on it. Since the electrons have a very small inertia, the net force on the electron fluid necessary to cause it to accelerate is much smaller than the  $\mathbf{J}_{E \times B}$  force. Thus in considering the force equation for the electron fluid, we obtain

$$j_{ey} \times B_x/c \sim -neE_z \gg nm_e dV_{ez}/dt. \quad (2)$$

For the ions, we have, in the normal direction,

$$nm_i V_{iz}(\partial V_{iz}/\partial z) = ne[V_{ix} B_y - V_{iy} B_x - E_z]/c - \partial P_i/\partial z. \quad (3)$$

In the limit that  $V_x$  and  $V_y$  are small, as is the case in the data presented for the thin current sheet near the x-line, then the primary agent operating on the ions is the electric field. We have

$$(m_i/e)V_{iz}(\partial V_{iz}/\partial z) - (1/ne)\partial P_i/\partial z \sim E_z \sim -(J_{ey} \times B_x)/nec. \quad (4)$$

The above equation illustrates that the charge separation electric field ( $E_z$ ) arises as a consequence of the Lorentz

force ( $\mathbf{j}_e \times \mathbf{B})/c$  on the electron fluid and its coupling to the ions in a manner consistent with maintaining quasi-neutrality. The electric field is responsible for the deceleration of the ion fluid (the convective derivative) through the structure and maintaining of the ion pressure gradient through its contribution to the confinement of trapped ions. Given that the electric potential drop is 4–6 keV and that the incident  $H^+$  bulk fluid slows down by about 400–600 km/s to about zero, we can estimate that the fluid convective derivative results in an energy change per  $H^+$  ion of about 1–2 keV over an 80 km scale. The force equation indicates the sum of the above two terms should balance the  $H^+$  pressure change. Thus, the ion pressure change should be about 5–7 keV per particle over 80 km. Thus the potential drop term balances the 70–80% of the ion pressure gradient and the convective derivative balances the other 20–30% of the ion pressure gradient. It should be noted that the  $O^+$  counterstreaming beams are also accelerated across the potential well increasing the  $O^+$  pressure by  $\sim 5$  keV per ion. In this case, it is to be expected that the electric potential nearly balances the  $O^+$  pressure with the convective derivative playing a smaller role.

[50] The direct effect of the magnetic field is on the electron fluid through the  $\mathbf{J}_e \times \mathbf{B}$  force which contains magnetic pressure and magnetic tension forces. These forces are coupled to the unmagnetized ions through the electric field. In this picture, the electrons produce the  $\mathbf{j}_e$  by  $\mathbf{E} \times \mathbf{B}$  drifting in the normal  $E_z$  component of the electric field. Under these circumstances,  $j_{ey} \sim necE_z/B_x$ . Thus the term on the right hand side of equation (4) independently gives the result  $(J_{ey} \times B_x)/nec \sim E_z$ . Spatial integration of this expression across the thin current sheet to the midplane of the current sheet and use of Amperes law gives the relation between the depth of the potential well, the magnetic field and total density of charge carriers,  $e\Delta\phi \sim (\Delta(B_x^2)/8\pi n) = (1/2)m_i V_A^2$ . This is the same value as the potential drop across a fast mode subcritical perpendicular shock which is characterized by a thickness of several electron inertial lengths, electrons that  $\mathbf{E} \times \mathbf{B}$  drift forming the current layer, and ions that are ballistically decelerated [*Tidman and Krall*, 1971]. Unlike the fast mode shock, in this case we have two back to back standing waves and the associated potential well.

[51] In the single particle picture, an ion accelerated across the potential drop is energized such that its streaming velocity inside the potential well is  $\sim V_{AH^+}$  for  $H^+$  ions, and  $V_{AO^+}$  for  $O^+$  ions. Since any ion accelerated through the potential well increases its potential energy by  $(\Delta(B_x^2)/8\pi n)$ , The total pressure difference (including the dynamic pressure) across the current layer may be calculated from the change in kinetic energy density for one particle. For the nearly constant density profile of the thin current sheet crossing, the pressure difference may be calculated as  $(n_{H^+} + n_{O^+}) (\Delta(B_x^2)/8\pi n_e) = (\Delta(B_x^2)/8\pi)$  where from quasi-neutrality  $n_e = n_{H^+} + n_{O^+}$ . Thus the potential drop in this approximation automatically produces the particle momentum flux gradient necessary to balance the magnetic pressure. Each ion makes the same contribution to the pressure. Since the  $O^+$  density is several times that of the  $H^+$  density, this simple scenario suggests that the  $O^+$  pressure dominates the  $H^+$  pressure by a factor of 4 or 5. As expected in a reconnection scenario, the power dissipated in ion

acceleration across the potential drop is provided by the inflow of Poynting flux. This may be most easily seen by considering a two dimensional geometry and noting that divergence of the Poynting flux is in the normal ( $z$ ) direction. The normal flux of particles into the potential drop is  $nV_z$ . The power dissipated across the potential drop per unit area is  $nV_z e\Delta\phi \sim nV_z \Delta(B_x^2)/8\pi n \sim E_{\text{tan}}(\Delta B_x)/4\pi = S_{\text{in}}$  where  $S$  is the Poynting flux through an area transverse to the normal. The magnetic field difference is evaluated immediately upstream and downstream of the small-scale potential drop. This oversimplified example is used to illustrate the consistency of the ion acceleration via the small scale potential well with a general reconnection energy flow; however, it is not intended to exclude other contributions to the energy balance and the force equations due to radiated wave energy and electron energization by microinstabilities. These contributions have yet to be experimentally assessed.

[52] A crucial question is how the ions are ejected into the outflow direction. A number of mechanisms could govern subsequent motion of the ions. Deflection of the ions in the outflow direction can occur because of ballistic motion and specular reflection off the diverging electrostatic walls of the standing wave funnel geometry. This motion converts the counterstreaming (along the normal or  $z$  direction) ion beams, into a jet of outflowing plasma moving in the  $x$  direction at the Alfvén velocity. In this scenario, the standing waves near the  $x$ -line behave much like a gas dynamic nozzle with ions reflecting off the electrostatic walls. Each reflection conserves energy and deflects the velocity of the ion in the  $x$  direction. Alternatively, ions can be ejected in the outflow direction by an electric field directed in the  $x$  direction [Biskamp, 2000] by turbulence. In principle, a wide variety of such mechanisms could exist. The nature of the ejection mechanism(s) for ions near the  $x$ -line is an outstanding experimental problem of reconnection dynamics.

#### 4.4. Equipotential Contours and Particle Trajectories

[53] Figure 14 (bottom) presents an idealized schematic of equipotential contours projected into the  $y$ - $z$  plane illustrating a possible local two-dimensional steady state structure of the nested large and small-scale potential wells. The purpose of the figure is to illustrate with a specific example how  $H^+$  ions can  $\mathbf{E} \times \mathbf{B}$  drift through the large-scale structure and be accelerated ballistically through the small-scale electric potential well, while oxygen ions are accelerated through both large- and small-scale structures. Electrons  $\mathbf{E} \times \mathbf{B}$  drift through both structures. This exercise does not include the effects of microturbulence, small-scale plasma structures, and parallel electric fields which can exist in these regions. The figure shows the trajectories of  $O^+$  ions,  $H^+$  ions, and electrons with selected energies through the potential structure. It does not show the warping of the current sheet seen over larger scales and associated with the kink-like wave. For simplicity, it depicts a symmetric potential structure between northern and southern tail lobe sides of the current sheet. Notice that electric field measurements along a hypothetical spacecraft trajectory through the center of this structure will produce a potential well structure similar to that shown in Figure 11b. At the upper and lower bounds of the diagram, the equipotentials are nearly vertical, modeling the dominance of the tangential component of the electric field in the upstream tail lobes. As the

current sheet is approached, the equipotentials are deflected to the left in a manner consistent with a large normal component of the electric field directed towards the midplane of the current sheet. As the immediate vicinity of the midplane current sheet is approached, the contours are deflected more horizontally and are closer together. This illustrates the intense small-scale potential well. Notice that the overall structure is consistent with conservation of the tangential component of the electric field across the structure. The figure also presents some representative trajectories of particles moving through the potential structure. In the northern upstream region (tail lobe), all three groups of charged particles  $\mathbf{E} \times \mathbf{B}$  drift into the current sheet. As the  $O^+$  ion approaches the current sheet, it is accelerated across the current sheet in a near ballistic trajectory since its gyroradius is large compared to the current sheet potential structure. It crosses 15–30 kV of potential drop and is trapped within the large-scale current sheet.  $H^+$  ions generally have a smaller gyroradius and for a range of energies can  $\mathbf{E} \times \mathbf{B}$  drift through the large-scale structure crossing fewer potential contours. The electrons, with a gyroradius of  $\sim 3$  km compared to the large-scale current sheet scale size of  $\sim 2000$  km, will  $\mathbf{E} \times \mathbf{B}$  drift throughout the large-scale current sheet and potential structure. When an  $H^+$  ion encounters the thin current sheet potential structure with a scale size of 100 km (much smaller than a typical 100 eV  $H^+$  gyroradius), it is ballistically accelerated across the small scale potential drop and is energized by 4–6 keV. The electrons  $\mathbf{E} \times \mathbf{B}$  drift across most of this structure and are energized by much less. The  $\mathbf{E} \times \mathbf{B}$  drift of the electrons ( $\sim 10,000$  km/s from the data) can be one of the major contributors to the current layer. When the electrons drift sufficiently close to the weak magnetic field region, they should become nonadiabatic and execute meandering orbits which also could contribute to the current layer.

[54] The steady state Poynting flux ( $\mathbf{E} \times \mathbf{B}$ ) flows on equipotential surfaces in a direction perpendicular to  $\mathbf{B}$ . Thus Figure 14 also provides insight into Poynting flux flow. Figure 14 illustrates that steady-state Poynting flux is very strongly diverted in the  $-y$  direction as it traverses the current sheet on its path to the current sheet midplane. There is an additional component of the Poynting flux in the outflow direction due to the Hall magnetic field perturbation and the normal component of the electric field. In this steady state picture, the existence of a tangential component of the electric field insures that all Poynting flux converges on the midplane/magnetic field reversal. Because the local magnetic field decreases as the current sheet midplane is approached, the electromagnet energy flux decreases as the midplane plane is approached. Globally, there is a divergence in the steady state Poynting flux. The major energy dissipation mechanism in these observations is the acceleration of the ion beams although other modes of energy transport also contribute. There is ample evidence in the data for higher time resolution electric and magnetic field fluctuations which complicate this illustrative picture.

#### 4.5. Relation of the Normal Component of the Electric Field to the Hall Magnetic Field Perturbation

[55] The normal component of the electric field and the Hall magnetic field perturbation are correlated and may be

under stood in several different but mutually consistent ways:

[56] 1. For a steady state, 2-D, planar structure in the normal incidence frame with a normal component of the electric field  $E_N$  (which is directed along  $z$ ), a constant tangential component of the electric field,  $E_Y$ , a constant normal component of the magnetic field,  $B_N$ ; and, a “Hall” magnetic field perturbation,  $B_Y$ , the relation  $\mathbf{E} \cdot \mathbf{B} = 0$  implies that:  $E_N(z) B_N + E_Y B_Y(z) \sim 0$  or

$$E_N(z) \sim -(E_Y/B_N) B_Y(z).$$

Thus there is a constant proportionality between  $E_N(z)$  and  $B_Y(z)$  which is  $(E_Y/B_N)$  or the deHoffman-Teller velocity. Deviations from perfect correlation may be the consequence of the fact that the shock structure is not completely planar, and the existence of finite parallel electric field. This relation is analogous to the equivalent relation for quasi-perpendicular fast mode shocks [Wygant *et al.*, 1987]. At the thin current sheet crossing observed by Spacecraft 4 nearest the x-line, the ratio  $E_N/B_Y \sim E_Y/B_N$  is 85 mV/m/5 nT corresponding to a local deHoffman Teller velocity of 10,000–15000 km/s or  $\sim 40 V_A$  (based on total mass density of  $O^+$  and  $H^+$ ) or  $\sim 10 V_{A_{H^+}} = B/(4\pi\rho_{H^+})^{1/2}$  (the Alfvén velocity derived from only the hydrogen mass density,  $\rho_{H^+}$ ). This is a very high value compared with previous observations and that assumed for analytic models. The value of the deHoffman-Teller velocity typically assumed in MHD scenarios is about  $\sim 1 V_A$  [Hughes, 1995; Cowley, 1986, and references therein]. Since the ion data show that both ion species are decoupled from  $\mathbf{E} \times \mathbf{B}$  velocity in this crossing, a more appropriate comparison is to the electron Alfvén velocity  $V_{Ae} = B/(4\pi\rho_e)^{1/2}$ , where  $\rho_e$  is the electron mass density. The deHoffman-Teller velocity is about  $\sim 0.25 V_{Ae}$ . Downstream of the Spacecraft 4 position, Spacecraft 3 measured a local deHoffman-Teller velocity of  $\sim 4000$  km/s. The decrease in this velocity with distance along the x axis is consistent with the “freezing in” of ions as the current sheet and potential structure gradually broaden to MHD scales. In this context, this ratio may be regarded as an indicator of proximity to the x-line.

[57] 2. The relation between  $E_N(z)$  and  $B_Y(z)$  might also be understood as a consequence of the fact that the magnetic field in the current layer is frozen into the electron flow velocity  $\mathbf{V}_E = |\mathbf{E} \times \mathbf{B}/B^2| \sim E_N/B_x$  [Mandt *et al.*, 1994]. Under these circumstances, to first-order, the magnetic field direction is tilted by an amount  $\sin\theta = B_Y/B_x = V_E/V_\phi = M_{Ae}$ , where  $M_{Ae}$  is the Mach number of the electron  $\mathbf{E} \times \mathbf{B}$  velocity relative to the phase velocity of an electron Alfvén wave- which is the wave transmitting the information on the tilt in the magnetic field down the magnetic field line. The tilt produces an out of plane (Hall) component of the magnetic field  $B_Y$ . In the case of nonadiabatic ions and completely adiabatic electrons, this wave is analogous to an Alfvén wave with only the electrons frozen on to the magnetic field line, and  $V_\phi = B/(4\pi n_e m_e)^{1/2} \sim 30,000$  km. Since  $V_e \sim E_N/B_x \sim 10,000$  km/s, the electron Mach number is estimated to be  $M_{Ae} \sim 0.2$ . Thus the peak value of  $B_Y$  should be  $\sim 3$  nT compared to the actual measured value of  $B_Y \sim 5$  nT obtained from Figure 3a. The difference in the estimated and measured value of  $B_Y$  can be

understood as the consequence of the uncertainties in density and in the value of  $E_N$ , and the inadequate approximation for  $V_\phi$  since even a small amount of ion loading expected for scale sizes several times the electron inertial length could decrease  $V_\phi$  by a factor of two or three and increase  $B_Y$  by the same factor.

## 5. Summary

[58] Cluster electric field and magnetic field data, and ion distribution functions were analyzed from tail current sheet crossings in the geomagnetic tail during an interval when the reconnection line retreated over the spacecraft during a major geomagnetic storm. Detailed analysis of one of the thinnest (half width  $\sim 3 c/\omega_{pe}$ ) current sheet crossings was presented. In addition, a statistical analysis of the structure of the electric field at larger width (half width  $> 15 c/\omega_{pe}$ ) current sheets was provided. The relation of these fields to ion decoupling and acceleration in the immediate vicinity of the x line was provided. Some of the observations presented in this paper provide support for the following conclusions:

[59] 1. At the smallest-scale current sheet observed, there was a bipolar electric field structure directed normal to the current sheet and an associated electrostatic potential well with a depth of 4–6 kV and a scale size of 3–5  $c/\omega_{pe}$ . The walls of the potential well coincide with the bifurcated current sheets. The width of the well increases with distance away from the x-line along the outflow direction creating a two-dimensional funnel geometry. Five other examples of subion inertial length bipolar electric field structures coinciding with current sheets have been found during the 15 min interval of 0940–0955. They are all observed when the normal vector has a large projection along the y GSE plane and the normal component of the electric field is detectable by the 2-D measurements.

[60] 2. Upstream ions are non-adiabatic in these small scale structures and are accelerated in near ballistic trajectories across the potential drop and into the midplane of the reconnection region and pick up an energy of  $K_i \sim e\phi = e \int \mathbf{E} \cdot d\mathbf{l}$  as they move across the electric field structure. This normal component of the electric field serves as the primary energization mechanism for ions of less than several keV in thin current sheets during reconnection, not displacement along the reconnection electric field. This mechanism is different from the Speiser mechanism which invokes a meandering drift in the magnetic field reversal region along the tangential electric field. The Speiser mechanism may dominate in other regimes, for example (1) at distances more than one to several ion inertial lengths ( $\sim 1000$  km) from the x-line where current sheet structures are broad compared to the convected gyroradius of an ion, (2) near the x-line for ions with energies much greater than the cross shock potential.  $O^+$  ions are likely to be shock accelerated over larger distances (x direction) along the standing shock-like structures than  $H^+$  because of their larger gyroradius.

[61] 3. Inside the small scale potential well, velocity space distributions show counterstreaming monoenergetic  $H^+$  beams with velocities of  $\sim 1000$  km/s with small thermal velocity spreads of 100–200 km/s. The ratio of thermal energy to beam energy is  $\sim 0.04$ . The relatively pristine nature of the observed beams may be the consequence of the fact that the bounce time in the electrostatic well is



$\sim 0.1$  s and the fact that electromagnetic instabilities acting on the beams have growth rates [Gary *et al.*, 1993] longer than an ion gyroperiod (6–60s). Thus in the thinnest current sheet, the beams can bounce at least several times and be ejected downstream before gyrating or thermalizing. All ions within the potential well participate in these counterstreaming beams. The data suggests that the counterstreaming ions provide an effective pressure in the fluid picture, which supports pressure balance across the diamagnetic cavity. In principle, both  $H^+$  and  $O^+$  should be accelerated across the potential drop, each ion picking up 4–6 keV of kinetic energy. Thus, both species contribute to pressure balance through gradients in particle kinetic energy density. An additional contribution to momentum flux balance comes from the deceleration of the fluid through the convective derivative.

[62] 4. The data suggests that this crossing was obtained sufficiently close to the x-line that the ion fluid had not yet accelerated up to the outflow velocity of  $\sim 1 V_{AH+}$  in the x direction observed at crossings before and after this event.

[63] 5. In the individual particle scenario, ions from the upstream regions north and south of the reconnection structure are accelerated through the potential structure of the standing waves and into the center of the potential well where they bounce. The confinement is largely due to the electrostatic potential walls with a smaller contributions from the surrounding large-scale potential well and magnetic gyration. Within the context of the fluid picture, there is a different behavior. Unlike individual ions, the ion fluid normal velocity decelerates to zero across the standing structure. This follows from the fact that inside the potential well the individual ion beams counterstream, resulting in a comparatively small center-of-mass velocity and a large pressure. In the fluid picture, the fluid deceleration may be understood as the consequence of a mismatch between  $\partial P_{zz}/\partial z$  which is directed outward along the normal and the normal electric field which is directed inward along the normal. Within the context of the MHD force equation, the electric field does not appear (since it is an internal force between the electron and ion fluids), and the pressure gradient is the dominant term supporting the  $J \times B$  of the strong diamagnetic cavity centered on the neutral line. Simple conservation of energy arguments indicate this acceleration scenario is powered by Poynting flux inflow associated  $S = c/4\pi(E_{tan}B_x)$  as expected for any reconnection process.

[64] 6. Evidence is provided that the small-scale potential structures discussed above are imbedded in a larger scale current sheet and an associated larger-scale electrostatic potential well. Statistical analysis of  $\sim 30$  current sheet crossings supports the existence of a larger-scale ( $\sim 2000$  km) component of the bipolar electric field oriented in the normal direction with an amplitude of 5–15 mV/m. The asymmetry (50%) of the well potential may be explained as an artifact of the “skimming” trajectory of the spacecraft through the current sheet and the two-dimensional electric field instrument. Alternatively, there could be some degree of intrinsic asymmetry to the structure associated with differences in the northern and southern hemisphere upstream parameters.

[65] 7. The data indicates that the large-scale potential well structure can accelerate (and trap) ions with gyro radii

of 2000 km and greater. Measurements show counterstreaming  $O^+$  beams with energies of  $\sim 20$  keV are present throughout the large-scale ( $\Delta z \sim 2000$  km) potential well. The energy of the  $O^+$  beams is comparable to that of the potential drops associated with the well.  $H^+$  ions (with their smaller gyro radii) are expected to mostly  $E \times B$  drift through this potential structure and encounter very little of this large potential drop.

[66] 8. When considering the motion of electrons through the electric potential structure discussed herein, in the absence of all other contributions to the electron motion, the electrons should be mostly adiabatic and  $E \times B$  drift through the structure, picking up much less energy than the ions. Thus, the estimates of density and  $E \times B$  velocity from the data indicate that the  $E \times B$  drifting electrons should provide a significant contribution (50–100%) to the current density in the cross-tail current sheet. Any remaining (inferred and unmeasured) contribution could be due to electrons in meandering orbits or due to pressure gradient terms and is limited to 0–50%. The peak  $E \times B$  velocity in the y direction is estimated to be  $EzBx/Bmag^2 \sim (80 \text{ mV/m}/8 \text{ nT}) \sim 10,000 \text{ km/s} \sim 0.25 V_{Ac}$ . There is a significant contribution to the x component of the  $E \times B$  velocity in the outflow direction (x) given by  $EzBy/|B|^2 \sim 8000 \text{ km/s} \sim 0.2 V_{Ac}$ . The electron energy associated with the (ordered)  $E \times B$  motion is  $\sim 0.6$  keV compared to the ion beam energy of  $\sim 5$  keV. There is evidence from 2-D pitch angle distribution functions at this event (not presented here) that the electrons have a much larger energy (1–2 keV) parallel to the magnetic field than perpendicular. Additional electron energization may result from a variety of mechanisms not discussed herein. These include from acceleration in small-scale wave fields; drift along the tangential component of the electric field; parallel electric field structures, and any smaller scale perpendicular shock-like electric field structures similar to those discussed here for  $H^+$  and  $O^+$  species.

[67] 9. Simultaneous passes through the reconnection structure at different distances along the outflow direction provide the first evidence that the standing structures including current sheets, electric field structures, and the potential well have a diverging geometry, as first proposed by Petschek [1964]. Evidence from the two spacecraft measurements indicate that the current sheet and electric field structure width broadens with distance downstream from the x-line, the electric fields become less intense, but the potential drops become somewhat larger (since the scale size of the electric field more than compensates for its decrease in magnitude). The ratio of the normal component of the electric field to the Hall magnetic field perturbation becomes smaller with distance from the x-line. The diamagnetic cavity is less deep. Enhancements in density within the current layer become appreciable with distance along the outflow direction.

[68] 10. An estimate of the cross current layer potential in the cold electron approximation for thin current sheets (smaller than an ion convected gyroradius) in which the  $E \times B$  drift of the electrons produces the cross-tail current is  $\Delta\phi \sim \Delta B^2/4\pi ne = \Delta (1/2) mV_A^2$  (see discussion section). This relation breaks down as electrons contribute to pressure gradients and their non- $E \times B$  motion contributes to the current layer and as the ions become

progressively more magnetized and  $\mathbf{E} \times \mathbf{B}$  drift canceling the current due to the electron  $\mathbf{E} \times \mathbf{B}$  drift.

[69] 11. A variety of scenarios exist for converting the counterstreaming motion of ions along the current sheet normal (z) into “jets” flowing along the outflow direction (x). The first is an “electrostatic nozzle.” The normal component of the electric field provides an electric field structure which for the ions defines a two dimensional “nozzle” which consist of two electric field walls which are inclined at the same opening angles (10–20 degrees) as standing slow mode shocks. Even in the absence of any other forces, individual ions accelerated into the “nozzle” may be quasi-trapped, bouncing between the electrostatic walls. With specular reflection and a diverging geometry for the electrostatic walls, each bounce converts motion along the normal direction to motion along the outflow direction. If the trajectories of many such individual ions are summed to construct fluid flow velocities, we can see that the flows are consistent with the formation of ion jets expected from the reconnection process and reminiscent of gas dynamic flow exiting diverging nozzles. A second mechanism for accelerating ions away from the x line in the outflow direction could be an electric field component in the x direction [Biskamp, 2000; Shay et al., 2001]. A third mechanism is essentially the Speiser mechanism. Since ions are confined to the mid plane bouncing along the normal (z) direction and drift in the magnetic field reversal region along the tangential component of the electric field. As a consequence of this displacement along the electric field, they are accelerated along the y direction. This velocity along with the Hall magnetic field perturbation produces a Lorentz force expelling the ion along the x direction  $F_{Lx} = (q/c)(V_y B_z - V_z B_y)$  [Speiser, 1965; Cowley, 1986; Hughes, 1995].

[70] **Acknowledgments.** Work on this paper supported by NASA contracts NAG5-12765, SA3589, NAG5-11868, and FDNAG5-11944-03/05. Magnetic field data analysis by Margaret Kivelson is gratefully acknowledged.

[71] Lou-Chuang Lee thanks James Drake and another reviewer for their assistance in evaluating this paper.

## References

- Andre, M., et al. (2001), Multi-spacecraft observations of broad band waves near the lower hybrid frequency of the earthward edge of the magnetopause, *Ann Geophys.*, **19**, 1471.
- Andre, M., A. Vaivads, S. C. Buchert, A. Fazakerley, and A. Lahiff (2004), Thin electron scale layers at the magnetopause, *Geophys. Res. Lett.*, **31**, L03803, doi:10.1029/2003GL018137.
- Angelopoulos, V., et al. (1994), Statistical characteristics of bursty bulk flow events, *J. Geophys. Res.*, **99**, 21,257.
- Arzner, K., and M. Scholer (2001), Kinetic structure of the post plasmoid plasma sheet during magnetotail reconnection, *J. Geophys. Res.*, **106**, 3827.
- Bale, S., F. S. Mozer, and T. Phan (2002), Observations of lower hybrid wave instability in the diffusion region at a reconnecting magnetopause, *Geophys. Res. Lett.*, **29**(24), 2180, doi:10.1029/2002GL016113.
- Balogh, A., et al. (2001), The Cluster Magnetic Field Investigation: Overview of in-flight performance and initial results, *Ann. Geophys.*, **19**, 1207.
- Bauer, T. M., W. Baumjohann, and R. A. Treumann (1995), Neutral sheet oscillations at substorm onset, *J. Geophys. Res.*, **100**, 23,737.
- Birn, J., et al. (2001), Geospace Environment Modeling (GEM) magnetic reconnection challenge, *J. Geophys. Res.*, **106**, 3715.
- Biskamp, D. (2000), *Magnetic Reconnection in Plasmas*, Cambridge Monogr. on Plasma Phys., Cambridge Univ. Press, New York.
- Cattell, C. A., and F. S. Mozer (1986), Experimental determination of the dominant wave mode in the active near-Earth magnetotail, *Geophys. Res. Lett.*, **13**, 221.
- Cattell, C., J. Wygant, F. S. Mozer, T. Okada, K. Tsuruda, S. Kokubun, and T. Yamamoto (1995), ISEE-1 and Geotail observations of low-frequency waves at the magnetopause, *J. Geophys. Res.*, **100**, 11,823.
- Cattell, C., et al. (2005), Cluster observations of electron holes in association with magnetotail reconnection and comparison to simulations, *J. Geophys. Res.*, **110**, A01211, doi:10.1029/2004JA010519.
- Cowley, S. W. H. (1986), Magnetic reconnection, in *Solar System Magnetic Fields*, edited by E. R. Priest, p. 121, Springer, New York.
- Drake, J. F., D. Biskamp, and A. Zeiler (1997), Break-up of the electron current during three dimensional magnetic reconnection, *Geophys. Res. Lett.*, **24**, 2921.
- Drake, J., M. Swisdak, C. Cattell, M. Shay, B. Rogers, and A. Zeiler (2003), Formation of electron holes and particle energization during magnetic reconnection, *Science*, **299**, 834.
- Gary, S. P. (1993), *Theory of Space Plasma Micro-Instabilities*, Cambridge Univ. Press, New York.
- Gekelman, W., R. L. Stenzel, and N. Wild (1982), Magnetic field line reconnection experiments: 3. Ion acceleration, flows, and anomalous scattering, *J. Geophys. Res.*, **87**, 101.
- Gustafson, G., et al. (1997), EFW instrument for CLUSTER, in *The CLUSTER and Phoenix Missions*, edited by C. P. Escoubert, C. T. Russell, and R. Schmidt, p. 31, Springer, New York.
- Hesse, M., D. Winske, and J. Birn (1998), On the ion scale structure of thin current sheets in the magnetotail, *Phys. Scr. T*, **74**, 63.
- Hesse, M., J. Birn, and M. Kuznetsova (2001), Collisionless magnetic reconnection: Electron processes and transport modeling, *J. Geophys. Res.*, **106**, 3737.
- Hones, E. W. (1979), Transient phenomena in the magnetotail and their relation to substorms, *Space Sci. Rev.*, **23**, 393.
- Hoshino, M., T. Mukai, Y. Yamamoto, and S. Kokubun (1998), Ion dynamics in magnetic reconnection: Comparison between numerical simulation and Geotail observations, *J. Geophys. Res.*, **102**, 4509.
- Hughes, J. (1995), Magnetic reconnection, in *Space Plasma Physics*, edited by M. Kivelson and C. T. Russell, Cambridge Univ. Press, New York.
- Karimabadi, H., W. Daughton, P. L. Pritchett, and D. Krauss-Varban (2003a), Ion-ion kink instability in the magnetotail: 1. Linear theory, *J. Geophys. Res.*, **108**(A11), 1400, doi:10.1029/2003JA010026.
- Karimabadi, H., P. L. Pritchett, W. Daughton, and D. Krauss-Varban (2003b), Ion-ion kink instability in the magnetotail: 2. Three-dimensional full particle and hybrid simulations and comparison with observations, *J. Geophys. Res.*, **108**(A11), 1401, doi:10.1029/2003JA010109.
- Kuznetsova, M. M., M. Hesse, and D. Winske (2001), Collisionless reconnection supported by nongyrotropic pressure effects in hybrid and particle simulations, *J. Geophys. Res.*, **106**, 3799.
- Lysak, R. (1998), The relation between electrostatic shocks and kinetic Alfvén waves, *Geophys. Res. Lett.*, **25**, 2089.
- Mandt, M. E., R. E. Denton, and J. F. Drake (1994), Transition to whistler mediated reconnection, *Geophys. Res. Lett.*, **21**, 73.
- Mozer, F. S., R. B. Torbert, U. V. Fahlson, C.-G. Falthammer, A. Gonfalone, A. Pederson, and C. T. Russell (1979), Direct observation of a tangential component of the electric field at the magnetopause, *Geophys. Res. Lett.*, **6**, 305.
- Mozer, F. S., S. D. Bale, and T. D. Phan (2002), Evidence of diffusion region at a subsolar magnetopause crossing, *Phys. Rev. Lett.*, **89**, 15002-1.
- Mozer, F. S., T. D. Phan, and S. D. Bale (2003), The complex three dimensional structure of the magnetopause, *Phys. Plasmas*, **10**, 2480.
- Nagai, T., M. Fujimoto, Y. Saito, S. Machida, T. Terasawa, R. Nakamura, T. Yamamoto, T. Mukai, A. Nishida, and S. Kokubun (1998), Structure and dynamics of magnetic reconnection with Geotail observations, *J. Geophys. Res.*, **103**, 4419.
- Nagai, T., I. Shinohara, M. Fujimoto, M. Hoshino, Y. Saito, S. Machida, and T. Mukai (2001), Geotail observations of the Hall current system: Evidence for reconnection in the magnetotail, *J. Geophys. Res.*, **106**, 25,929.
- Nakamura, M., M. Fujimoto, and K. Maezawa (1998), Ion dynamics and resultant velocity space distribution in the course of magnetotail reconnection, *J. Geophys. Res.*, **103**, 4531.
- Oieroset, M., et al. (2001), In situ detection of collisionless reconnection in the Earth's magnetotail, *Nature*, **412**, 414.
- Paschmann, G., et al. (1979), Plasma acceleration at the Earth's magnetopause: Evidence for reconnection, *Nature*, **282**, 243.
- Phan, T. D., and G. Paschmann (1996), Low-latitude dayside magnetopause and boundary layer for high magnetic shear: 1. Structure and motion, *J. Geophys. Res.*, **101**, 7801.
- Phan, T. D., G. Paschmann, and B. U. Ö. Sonnerup (1996), Low-latitude dayside magnetopause and boundary layer for high magnetic shear: 2. Occurrence of magnetic reconnection, *J. Geophys. Res.*, **101**, 7817.



- Petschek, H. E. (1964), Magnetic field annihilation, in *AAS/NASA NASA Symposium on the Physics of Solar Flares*, edited W. N. Ness, pp. 425–437, NASA, Washington, D.C.
- Pritchett, P. L. (2001), Geospace Environment Modeling magnetic reconnection challenge: Simulations with a full particle electromagnetic code, *J. Geophys. Res.*, **106**, 3783.
- Pritchett, P. L., and F. V. Coroniti (1996), The role of the drift-kink mode in destabilizing thin current sheets, *J. Geomagn. Geoelectr.*, **48**, 833.
- Pritchett, P. L., and F. V. Coroniti (1997), Interchange and kink modes in the near Earth plasma sheet and their associated plasma flows, *Geophys. Res. Lett.*, **24**, 2925.
- Reme, H., et al. (1997), The Cluster Ion Spectrometry (CIS) experiment, in *The CLUSTER and Phoenix Missions*, edited by C. P. Escoubert, C. T. Russell, and R. Schmidt, pp. 305–330, Springer, New York.
- Reiff, P. H., R. W. Spiro, and T. W. Hill (1981), Dependence of the polar cap potential on interplanetary parameters, *J. Geophys. Res.*, **86**, 7639.
- Ricci, P., G. Lapenta, and J. U. Brackbill (2002), GEM reconnection challenge: Implicit kinetic simulations with the physical mass ratio, *Geophys. Res. Lett.*, **29**(23), 2088, doi:10.1029/2002GL015314.
- Rogers, B. N., R. E. Denton, J. F. Drake, and M. A. Shay (2001), Role of dispersive waves in collisionless magnetic reconnection, *Phys. Rev. Lett.*, **87**, 195004.
- Runov, A., et al. (2003a), Current sheet structure near magnetic X-line observed by Cluster, *Geophys. Res. Lett.*, **30**(11), 1579, doi:10.1029/2002GL016730.
- Runov, A., R. Nakamura, W. Baumjohann, T. L. Zhang, M. Volwerk, and H.-U. Eichelberger (2003b), Cluster observations of bifurcated current sheets, *Geophys. Res. Lett.*, **30**(2), 1036, doi:10.1029/2002GL016136.
- Scauder, J. D., F. S. Mozer, N. C. Maynard, and C. T. Russell (2002), Fingerprints of collisionless reconnection at the separator: 1. Ambipolar fingerprints, *J. Geophys. Res.*, **107**(A10), 1294, doi:10.1029/2001JA000126.
- Sergeev, V., V. Angelopoulos, C. Carlson, and P. Sutcliffe (1998), Current sheet measurements with a flapping plasma sheet, *J. Geophys. Res.*, **102**, 9177.
- Sergeev, V., et al. (2003), Current sheet flapping motion and structure observed by Cluster, *Geophys. Res. Lett.*, **30**(6), 1327, doi:10.1029/2002GL016500.
- Shay, M. A., J. F. Drake, R. E. Denton, and D. Biskamp (1998), Structure of the dissipation region during collisionless magnetic reconnection, *J. Geophys. Res.*, **103**, 9165.
- Shay, M. A., et al. (2001), Alfvénic magnetic field reconnection and the Hall term, *J. Geophys. Res.*, **106**, 3759.
- Song, Y., and R. L. Lysak (1995), MHD mesoscale interactions at the magnetopause and driven reconnection, in *Physics of the Magnetopause*, *Geophys. Monogr. Ser.*, vol. 90, edited by P. Song, B. U. O. Sonnerup, and M. F. Thomsen, p. 349, AGU, Washington, D. C.
- Sonnerup, B. U. O. (1979), Magnetic field reconnection in *Solar System Plasma Physics*, vol. 3, edited by L. T. Lanzerotti, C. F. Kennel, and E. N. Parker, pp. 45–108, North Holland, New York.
- Sonnerup, B. U. O., et al. (1981), Evidence for magnetic field reconnection at the Earth's magnetopause, *J. Geophys. Res.*, **86**, 10,049.
- Speiser, T. W. (1965), Particle trajectories in model current sheets: 1. Analytic solutions, *J. Geophys. Res.*, **70**, 4219.
- Stenzel, R. L., W. Gekelman, and N. Wild (1982), Magnetic field line reconnection experiments 4: Resistivity, heating, and energy flow, *J. Geophys. Res.*, **87**, 111.
- Stenzel, R. L., W. Gekelman, and N. Wild (1983), Magnetic field line reconnection experiments, current disruption and double layers, *J. Geophys. Res.*, **88**, 4793.
- Syrovatskii, S. I. (1971), Formation of current sheets in a plasma with a frozen-in strong magnetic field, *Sov. Phys. JETP*, **33**, 933.
- Tidman, D. A., and N. A. Krall (1971), *Shock Waves in Collisionless Plasmas*, John Wiley, Hoboken, N. J.
- Vaivads, A., M. Andre, S. C. Buchert, J. E. Wahlund, A. N. Fazakerley, and N. Cornilleau-Wehrin (2004), Cluster observations of lower hybrid turbulence within thin layers near the magnetopause, *Geophys. Res. Lett.*, **31**, L03804, doi:10.1029/2003GL018142.
- Volwerk, M., K.-H. Glassmeier, A. Runov, W. Baumjohann, R. Nakamura, T. L. Zhang, B. Klecker, A. Balogh, and H. Reme (2003), Kink mode of the oscillation of a current sheet, *Geophys. Res. Lett.*, **30**(6), 1320, doi:10.1029/2002GL016467.
- Wygant, J. R., F. S. Mozer, and R. Torbert (1983), Comparison of S3-3 polar cap potential drops to models of magnetopause reconnection, *J. Geophys. Res.*, **88**, 5727.
- Wygant, J. R., M. Bensadoun, and F. S. Mozer (1987), Electric field measurements at a subcritical oblique bow shock crossing, *J. Geophys. Res.*, **9**, 11,109.
- Wygant, J. R., J. Dombek, R. Lysak, J. McFadden, C. Carlson, F. Mozer, H. Reme, E. Lucek, and M. Andre (2003), Cluster observations of the electric field structure of the reconnection region in the plasma sheet: an electrostatic nozzle, *Geophys. Res. Abstr.*, **5**, 13,835.
- Zeiler, A., D. Biskamp, J. F. Drake, B. N. Rodgers, and M. A. Scholer (2002), Three dimensional particle simulations of collisionless magnetic reconnection, *J. Geophys. Res.*, **107**(A9), 1230, doi:10.1029/2001JA000287.
- Zhang, T. L., W. Baumjohann, R. Nakamura, A. Balogh, and K.-H. Glassmeier (2002), A wavy twisted neutral sheet observed by CLUSTER, *Geophys. Res. Lett.*, **29**(19), 1899, doi:10.1029/2002GL015544.

M. Andre, Swedish Institute of Space Physics, Uppsala Division, Uppsala, Sweden.

A. Balogh and E. A. Lucek, Blackett Laboratory, Imperial College, Prince Consort Road, London, SW7 2B7, UK.

C. A. Cattell, J. Dombek, R. Lysak, Y. Song, and J. R. Wygant, School of Physics and Astronomy, University of Minnesota, Minneapolis, MN 55455, USA. (wygant@ham.space.umn.edu)

C. W. Carlson, J. McFadden, F. S. Mozer, and G. Parks, Space Sciences Laboratory, University of California, Berkeley, CA 94720, USA.

M. Hesse, NASA Goddard Space Flight Center, Greenbelt, MD, USA.

C. Mouikis, University of New Hampshire, Durham, NH, USA.

H. Reme, CESR, Toulouse, France.